

## Climate and carbon cycle changes from 1850 to 2100 in MPI-ESM simulations for the Coupled Model Intercomparison Project phase 5

Marco A. Giorgetta,<sup>1</sup> Johann Jungclaus,<sup>1</sup> Christian H. Reick,<sup>1</sup> Stephanie Legutke,<sup>2</sup> Jürgen Bader,<sup>1</sup> Michael Böttiger,<sup>2</sup> Victor Brovkin,<sup>1</sup> Traute Crueger,<sup>1</sup> Monika Esch,<sup>1</sup> Kerstin Fieg,<sup>2</sup> Ksenia Glushak,<sup>2</sup> Veronika Gayler,<sup>1</sup> Helmuth Haak,<sup>1</sup> Heinz-Dieter Hollweg,<sup>2</sup> Tatiana Ilyina,<sup>1</sup> Stefan Kinne,<sup>1</sup> Luis Kornblueh,<sup>1</sup> Daniela Matei,<sup>1</sup> Thorsten Mauritsen,<sup>1</sup> Uwe Mikolajewicz,<sup>1</sup> Wolfgang Mueller,<sup>1</sup> Dirk Notz,<sup>1</sup> Felix Pithan,<sup>1</sup> Thomas Raddatz,<sup>1</sup> Sebastian Rast,<sup>1</sup> Rene Redler,<sup>1</sup> Erich Roeckner,<sup>1</sup> Hauke Schmidt,<sup>1</sup> Reiner Schnur,<sup>1</sup> Joachim Segschneider,<sup>1</sup> Katharina D. Six,<sup>1</sup> Martina Stockhausen,<sup>2</sup> Claudia Timmreck,<sup>1</sup> Jörg Wegner,<sup>2</sup> Heinrich Widmann,<sup>2</sup> Karl-H. Wieners,<sup>1</sup> Martin Claussen,<sup>1,3</sup> Jochem Marotzke,<sup>1</sup> and Bjorn Stevens<sup>1</sup>

Received 31 July 2012; revised 3 June 2013; accepted 11 June 2013.; published 17 September 2013

[1] The new Max-Planck-Institute Earth System Model (MPI-ESM) is used in the Coupled Model Intercomparison Project phase 5 (CMIP5) in a series of climate change experiments for either idealized CO<sub>2</sub>-only forcing or forcings based on observations and the Representative Concentration Pathway (RCP) scenarios. The paper gives an overview of the model configurations, experiments related forcings, and initialization procedures and presents results for the simulated changes in climate and carbon cycle. It is found that the climate feedback depends on the global warming and possibly the forcing history. The global warming from climatological 1850 conditions to 2080–2100 ranges from 1.5°C under the RCP2.6 scenario to 4.4°C under the RCP8.5 scenario. Over this range, the patterns of temperature and precipitation change are nearly independent of the global warming. The model shows a tendency to reduce the ocean heat uptake efficiency toward a warmer climate, and hence acceleration in warming in the later years. The precipitation sensitivity can be as high as 2.5% K<sup>-1</sup> if the CO<sub>2</sub> concentration is constant, or as small as 1.6% K<sup>-1</sup>, if the CO<sub>2</sub> concentration is increasing. The oceanic uptake of anthropogenic carbon increases over time in all scenarios, being smallest in the experiment forced by RCP2.6 and largest in that for RCP8.5. The land also serves as a net carbon sink in all scenarios, predominantly in boreal regions. The strong tropical carbon sources found in the RCP2.6 and RCP8.5 experiments are almost absent in the RCP4.5 experiment, which can be explained by reforestation in the RCP4.5 scenario.

**Citation:** Giorgetta, M. A., et al. (2013), Climate and carbon cycle changes from 1850 to 2100 in MPI-ESM simulations for the Coupled Model Intercomparison Project phase 5, *J. Adv. Model. Earth Syst.*, 5, 572–597, doi:10.1002/jame.20038.

### 1. Introduction

[2] Model intercomparison projects have become an important method to assess the uncertainty and robustness of model predictions where no reference solutions are known. This method has been used increasingly since the late 1980s [Cess *et al.*, 1989; Gates *et al.*, 1999; Lambert and Boer, 2001], especially for the assessment

of climate change in which the coupled model intercomparison project (CMIP) has come to play an important role. Phase 5 (CMIP5) of this project [Taylor *et al.*, 2012], thus follows on previous CMIPs and provides a new experimental framework that addresses traditional topics of CMIP, as for example climate change projections for scenarios of the future, as well as new topics, as for instance decadal climate prediction. An important addition to CMIP5 was the inclusion of idealized simulations designed to advance understanding.

[3] At the Max-Planck-Institute for Meteorology, CMIP5 was seen as an opportunity to merge a number of developments and define a new model system and test our understanding of its behavior. The resulting Max-Planck-Institute Earth System Model (MPI-ESM) has been employed in a large number of CMIP5 experiments. The goal of this article is to provide an overview

<sup>1</sup>Max-Planck-Institut für Meteorologie, KlimaCampus Hamburg, Germany.

<sup>2</sup>Deutsches Klimarechenzentrum, KlimaCampus, Hamburg, Germany.

<sup>3</sup>Meteorologisches Institut, Universität Hamburg, KlimaCampus, Hamburg, Germany.

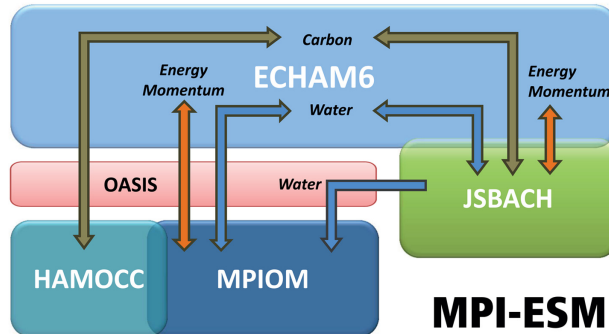


**Figure 1.** Schematic view of MPI-ESM: Colored boxes show the model components: ECHAM6 is the atmospheric general circulation model, which is directly coupled to the JSBACH land model that describes physical and biogeochemical aspects of soil and vegetation. MPIOM is the ocean general circulation model, which includes the HAMOCC model for the marine biogeochemistry. OASIS is the coupler program, which aggregates, interpolates, and exchanges fluxes and state variables once a day between ECHAM6+JSBACH and MPIOM+HAMOCC. The coupler exchanges fluxes for water, energy, momentum, and CO<sub>2</sub>.

of the model system and to describe the basic characteristics of climate change under idealized forcing as well as complex forcing for the past, based on observations, and for the future, based on scenarios. The focus of this study is on climate feedbacks, climate sensitivity, and the climate response. Both, physical aspects and the carbon budgets for the biogeochemical aspects of the model are investigated, making extensive use of idealized experiments as well as of the scenario simulations, in which the model is forced more realistically. For the realistic forcing of the historical past and the envisioned future scenarios, which are designed to explore a wide range of possible climates, the question will be addressed whether the spatial structure of changes with respect to the reference climate depends on the amplitude of the global mean change and whether the global mean change corresponds to the change expected from simplified experiments. As CMIP5 makes use of the new Representative Concentration Pathway (RCP) scenarios [Moss et al., 2010; van Vuuren et al., 2011a], which account for climate policies and span a wider range of developments than those of the Special Report on Emissions Scenarios (SRES) [Nakicenovic et al., 2000], the paper also addresses the question whether the goal of the most ambitious mitigation scenarios, to keep global warming below 2°C compared to 1850, can be reached in this model system. Related to this, we address the question, whether the implied anthropogenic CO<sub>2</sub> emissions diagnosed from the MPI-ESM simulations under different RCP concentration scenarios match the emissions that were originally used in integrated assessment models (IAM) to construct these scenarios. Deviations of these implied (or compatible) emissions in concentration driven scenario experiments from the original emissions would hint at systematic

differences in the CO<sub>2</sub> uptake by land and ocean between MPI-ESM and the different IAMs used to construct the RCP scenarios.

[4] The paper is organized as follows: section 2 introduces the model system. Sections 3 and 4 explain the experiments used in this study and the climate forcing imposed for the historical and scenario experiments. Section 5 discusses the results obtained from the experiments, addressing first systematic biases in the historical climate simulation, and then the changing climate in idealized and RCP-forced experiments. Section 6 is dedicated to changes in the carbon cycle of the historical and RCP-forced experiments. Section 7 summarizes and concludes.

## 2. Max-Planck-Institute Earth System Model

### 2.1. Model Structure

[5] The MPI-ESM consists of the coupled general circulation models for the atmosphere and the ocean, ECHAM6 [Stevens et al., 2013] and MPIOM [Jungclaus et al., 2013], and the subsystem models for land and vegetation JSBACH [Reick et al., 2013; Schneck et al., 2013] and for the marine biogeochemistry HAMOCC5 [Ilyina et al., 2013], respectively (Figure 1). Through the inclusion of these process models, the carbon cycle has been added to the model system. This constitutes the largest conceptual difference between MPI-ESM and its predecessor model ECHAM5/MPIOM [Jungclaus et al., 2006] that has been used for CMIP3. Earlier versions of the ECHAM5/MPIOM with an interactive carbon cycle have already been employed for the analysis of the climate–carbon cycle feedback [Friedlingstein et al., 2006], the estimation of compatible anthropogenic CO<sub>2</sub> emissions [Roeckner et al., 2011; Johns et al., 2011] and for simulations of the last millennium [Jungclaus et al., 2010]. In contrast to these earlier versions of the MPI coupled modeling system, the JSBACH component of MPI-ESM has been extended by a component for the climate-consistent development of the geographic distribution of vegetation, commonly called “dynamic vegetation” [Brovkin et al., 2009; Reick et al., 2013]. In addition the model for anthropogenic land-cover change was replaced by the land use transition approach by Hurtig et al. [2006] [see Reick et al., 2013]. All carbon fluxes from natural vegetation and soils [Schneck et al., 2013], as well as from anthropogenic land use and land use change [Pongratz et al., 2009] are simulated consistently.

[6] ECHAM6 [Stevens et al., 2013] is a new version of the ECHAM series of atmospheric general circulation models and was developed on the basis of ECHAM5 [Roeckner et al., 2003, 2006]. The most significant differences between ECHAM5 and ECHAM6 concern the radiation schemes, the computation of surface albedo, and the triggering condition for convection. The shortwave (SW) scheme has been replaced by the SW rapid radiation transfer model for GCMs (RRTMG-SW) that is based on the correlated-k method, like the corresponding RRTMG-LW scheme [Iacono et al., 2008]. The surface albedo scheme has been improved, accounting now

**Table 1.** MPI-ESM Configurations Used for CMIP5<sup>a</sup>

MPI-ESM Configuration	ECHAM6 Resolution	MPIOM Resolution	JSBACH Vegetation	Orbit
LR	T63/1.9° L47	GR15 L40	Dynamic	VSOP87
MR	T63/1.9° L95	TP04 L40	Dynamic	VSOP87
P	T63/1.9° L47	GR15 L40	Prescribed	Kepler

<sup>a</sup>T63 is a triangular truncation at wave number 63.

for solar zenith angle dependence over open water, for melt ponds on sea ice, as well as for snow covered land [Roeckner *et al.*, 2012]. The triggering condition for convection is no longer based on a constant temperature increment for probing the possibility of convective updrafts, but on the predicted variance of the virtual potential temperature [Stevens *et al.*, 2013, section 3.2.1]. Further ECHAM6 unifies the tropospheric ECHAM5 [Roeckner *et al.*, 2006] and the vertically extended Middle Atmosphere ECHAM5 [Manzini *et al.*, 2006]. The formulation of MPIOM has remained unchanged, except for the adaptations to high-resolution grids [Jungclaus *et al.*, 2013]. Changes in HAMOCC are minor and detailed in Ilyina *et al.* [2013].

## 2.2. Coupling

[7] The coupling procedure in MPI-ESM has remained unchanged compared to that in ECHAM5/MPIOM [Jungclaus *et al.*, 2006], except for an additional CO<sub>2</sub> coupling due to the carbon cycle. The coupling procedure distinguishes different time scales, dependent on the processes and components. The coupling at the interfaces between atmosphere and land processes, and between atmosphere and sea ice occurs at the atmospheric time step, which is also the time step of the land processes, except for the dynamic vegetation, which is updated once a year.

[8] The coupling between atmosphere and ocean as well as land and ocean, the latter by river runoff, occurs once a day. This coupling depends on surface fluxes of water, energy, momentum, and CO<sub>2</sub>, computed at the atmospheric time step, based on the actual atmospheric state and the mean ocean state of the last coupling interval. The daily mean fluxes, sent to the ocean model at the coupling time step, are then used as ocean-surface forcing over the following daily coupling interval. No flux adjustment is applied. The coupling between ocean dynamics and marine biogeochemistry occurs at the ocean time step.

[9] As the atmosphere and the ocean are discretized on different grids, a transformation of ocean state variables (sea surface temperature (SST) and ice cover) to the atmospheric grid and of surface fluxes to the ocean grid is needed. The transformation makes use of the conservative remapping functions of the spherical coordinate remapping and interpolation package (SCRIP) [Jones, 1999], which is embedded in the OASIS3 coupler [Valcke, 2013]. First-order conservative remapping is used for scalar quantities, but second order for wind stress.

[10] River runoff is calculated by the horizontal discharge model of Hagemann and Dümenil-Gates [2003]. It interpolates precipitation over land onto a 0.5° ×

0.5° grid, on which river catchments are defined. The runoff between cells is modeled based on resistances. The water flux at the continental discharge cells is passed back to the closest atmospheric grid cell with ocean surface at the coast, and passed through the OA-SIS3 coupler to the ocean model.

## 2.3. Model Configurations

[11] The model system has been developed for a variety of configurations (Table 1) differing in resolution of ECHAM6 or MPIOM (MPI-ESM-LR, -MR) or setup of orbit and vegetation (MPI-ESM-P). Of these configurations, the low resolution (LR) version of MPI-ESM (MPI-ESM-LR) has been used across a wide range of CMIP5 simulations to allow inferences across the whole experimental design of CMIP5. The mixed resolution (MR) version of MPI-ESM (MPI-ESM-MR), with higher vertical resolution in the atmosphere and higher horizontal resolution in the ocean, was used for a similar set of CMIP5 experiments, though with fewer realizations and fewer start dates for decadal predictions. Moreover, it is not used at all for experiments driven by CO<sub>2</sub> emissions. MPI-ESM-P was used for CMIP5 paleo experiments and a subset of long-term core experiments.

[12] The LR configuration uses for the atmosphere a T63/1.9° horizontal resolution and 47 hybrid sigma-pressure levels, and for the ocean a bipolar grid with 1.5° resolution (near the equator) and 40 z-levels. The poles of the ocean model are moved to Greenland and to the coast of the Weddell Sea by a conformal mapping of the geographical grid. MPI-ESM-LR has the same spatial resolutions in the atmosphere and ocean as ECHAM5/MPIOM used for CMIP3, except for the vertical grid in the atmosphere. The L47 grid extends to 0.01 hPa, while the L31 grid of ECHAM5 extended to 10 hPa. Between the surface and 100 hPa, however, both grids are identical. This vertical extension of the atmospheric grid includes for the first time the stratosphere in CMIP simulations at MPI-M, in order to capture the high variability of the high latitude circulation in the middle atmosphere, which dynamically influences the tropospheric circulation below [Karpechko and Manzini, 2012]. The time steps in the atmosphere and in the ocean are 600 and 4320 s, respectively.

[13] The MR configuration doubles the number of levels in the atmosphere from 47 to 95 and decreases the horizontal grid spacing of the ocean from nominally 1.5° to 0.4°, compared to the LR configuration. This ocean grid is a tripolar quasi-isotropic grid with two northern poles in Siberia and Canada and the third pole at the South Pole. The increased vertical resolution in

**Table 2.** CMIP5 Experiments Used in This Study<sup>a</sup>

CMIP5 Experiment Name	CMIP5 Experiment Number	Years	Reference
<i>piControl</i>	3.1	1000	<i>Giorgetta et al.</i> [2012a]
<i>abrupt4xCO<sub>2</sub></i>	6.3	150	<i>Giorgetta et al.</i> [2012b]
<i>1pctCO<sub>2</sub></i>	6.1	150	<i>Giorgetta et al.</i> [2012c]
<i>historical</i>	3.2	1850–2005 (3×)	<i>Giorgetta et al.</i> [2012d]
<i>amip</i>	3.3	1979–2008 (3×)	<i>Giorgetta et al.</i> [2012e]
<i>rcp26</i>	4.3	2006–2100 (3×)	<i>Giorgetta et al.</i> [2012f]
	4.3 L	2101–2300 (1×)	
<i>rcp45</i>	4.2	2006–2100 (3×)	<i>Giorgetta et al.</i> [2012g]
	4.2 L	2101–2300 (1×)	
<i>rcp85</i>	4.1	2006–2100 (3×)	<i>Giorgetta et al.</i> [2012h]
	4.3 L	2101–2300 (1×)	
<i>esmControl</i>	5.1	1000	<i>Reick et al.</i> [2012a]
<i>esmHistorical</i>	5.2	1850–2005 (3×)	<i>Reick et al.</i> [2012b]
<i>esmrcp85</i>	5.3	2006–2100 (1×)	<i>Reick et al.</i> [2012c]

<sup>a</sup>CMIP5 experiment names are defined in Appendix 1.1 of *Taylor et al.* [2012] and experiment numbers in *Taylor et al.* [2009]. Where more than one realization exists, the ensemble size is indicated in the “Years” column, e.g. (3×). References refer directly to the experiments.

the atmosphere allows for the resolution of large-scale tropical waves and wave–mean flow interaction, which is essential for the simulation of the quasi-biennial oscillation [*Giorgetta et al.*, 2006; *Krismeyer et al.*, 2013]. The higher horizontal resolution of the tripolar quasi-isotropic ocean grid makes the MPIOM model “eddy permitting” for most regions. The time steps in the atmosphere and ocean are 450 and 3600 s, respectively.

[14] The P configuration, used for the paleo simulations, is identical to the LR configuration with the exception of the orbital parameters which are prescribed rather than calculated from the internal calendar, and of the use of a prescribed sequence of global maps for vegetation and land-use from *Pongratz et al.* [2008] instead of using the dynamic vegetation and land use transitions.

[15] All model configurations were tuned in order to minimize biases in selected variables of the climate system. The tuning targets for the physical climate and the tuning procedure, which makes use of the uncoupled *amip* experiment [*Stevens and Bony*, 2013] and the coupled *piControl* experiment (see below), is described in *Mauritsen et al.* [2012]. Additional tuning steps were carried out to calibrate the carbon cycle as detailed in section 6.1. This biogeochemical tuning made use of the model setup for the *piControl* and *historical* simulations.

### 3. Experiments

[16] The following analysis relates to several CMIP5 experiments used to evaluate the model performance compared to observations, as the uncoupled *amip* experiment and the coupled *historical* experiment, or to analyze the climate change and its characteristics under different boundary conditions, as the idealized *abrupt4xCO<sub>2</sub>* and *1pctCO<sub>2</sub>* experiments or the *rcp* experiments (Table 2). Most of the experiments presented here are based on MPI-ESM-LR model.

#### 3.1. piControl

[17] The preindustrial control simulation *piControl* has a total length of 1000 years. The forcing is constant in time, with constant orbital parameters at 1850 values,

constant spectral solar irradiance computed as average over the solar cycle of the years 1844–1856, well-mixed greenhouse gas concentrations kept fixed at their values of the year 1850, and monthly ozone concentrations corresponding to the averaged for the 11 years from 1850 to 1860, i.e., again averaging over the length of a solar cycle. Aerosol forcing accounts for tropospheric natural aerosols only. Volcanic aerosol forcing is not present. The model setup for the *piControl* experiment was used for the development and the final tuning of MPI-ESM.

#### 3.2. abrupt4xCO<sub>2</sub>

[18] This idealized experiment was chosen for CMIP5 to analyze the climate sensitivity of a climate model following *Gregory et al.* [2004]. It is initialized from the *piControl* experiment and extends over 150 years with a constant CO<sub>2</sub> concentration that is quadrupled relative to that used in *piControl*. All other forcings are as in *piControl*.

#### 3.3. 1pctCO<sub>2</sub>

[19] *1pctCO<sub>2</sub>* is an idealized experiment for the analysis of the transient climate response to increasing CO<sub>2</sub> concentration alone. The *1pctCO<sub>2</sub>* experiment is initialized from the same *piControl* state as *abrupt4xCO<sub>2</sub>*. The integration also extends over 150 years with an annual 1% increase in CO<sub>2</sub> concentration, resulting in doubled and quadrupled CO<sub>2</sub> concentrations after approximately 70 and 140 years, respectively. All other forcings are as in *piControl*.

#### 3.4. Historical

[20] The *historical* experiment aims at the simulation of the climate from 1850 to 2005 under the influence of natural and anthropogenic forcings derived from observations. Three realizations of the historical experiment exist for MPI-ESM-LR and MPI-ESM-MR, differing in the initial state only. For MPI-ESM-LR, the realizations r1, r2, and r3 start from the end of the years 1880, 1980, and 1920, respectively, of the related *piControl* experiment. For the MPI-ESM-MR, they start from the end of the years 1850, 1900, and 1965, respectively, of

their corresponding *piControl* experiment. The natural forcing includes variations of the Earth orbit, variability in spectral solar irradiance, seasonally varying natural tropospheric aerosols, and stratospheric aerosols from volcanic eruptions. The latter decay to zero after the Pinatubo eruption of 1991. The anthropogenic forcing includes five well-mixed greenhouse gases CO<sub>2</sub>, CH<sub>4</sub>, N<sub>2</sub>O, CFC-11, and CFC-12 as well as O<sub>3</sub> and anthropogenic sulfate aerosols. The latter two are spatially and seasonally resolved. Further, anthropogenic land use change acts on surface properties and on the carbon cycle. More details on the forcings are given below. The model setup for the *historical* experiment was used for the tuning of the land carbon cycle.

### 3.5. *amip*

[21] The *amip* experiment is integrated from 1979 to 2008 using the same boundary conditions for atmosphere and land as the *historical* experiment up to 2005. For the following 3 years 2006–2008 the forcing of the RCP4.5 scenario has been applied. The boundary conditions for sea surface temperature and sea ice concentration (PCMDI, <http://www-pcmdi.llnl.gov/projects/amip/>) linearly interpolated between midpoints of months to the actual time in the model. There exist three realizations of the *amip* experiment.

### 3.6. *rcp26*, *rcp45*, and *rcp85*

[22] These experiments continue from the historical experiment until 2100, using the RCP concentration scenarios developed by Moss *et al.* [2010]. MPI-ESM was used to calculate projections for RCP2.6 [Van Vuuren *et al.*, 2011b], RCP4.5 [Thomson *et al.*, 2011], and RCP8.5 [Riahi *et al.*, 2011]. Three realizations exist for each of these RCP experiments, continuing the three realizations of the historical experiment. The natural forcing includes variations of the Earth orbit, variability in spectral solar irradiance and seasonally varying natural tropospheric aerosols. In addition, the assumption is made that no volcanic aerosols are present after 2005.

[23] The CMIP5 experiment protocol also includes extensions of *rcp26*, *rcp45*, and *rcp85* until 2300, based on the extended concentrations pathway (ECP) scenarios of Meinshausen *et al.* [2011]. Only the first realization of each of the *rcp* experiments is continued, however.

### 3.7. *esmControl*, *esmHistorical*, and *esmrp85*

[24] *esmControl*, *esmHistorical*, and *esmrp85* are identical to *piControl*, *historical*, and *rcp85*, respectively, except for the atmospheric CO<sub>2</sub> concentration, which is simulated instead of prescribed. The CO<sub>2</sub> concentration results from prescribed anthropogenic CO<sub>2</sub> emissions and land use change, the surface exchange of CO<sub>2</sub> between atmosphere and land or atmosphere and ocean, and the atmospheric transport. As the predicted CO<sub>2</sub> concentration depends on the climate state, the *esm* simulations allow for carbon climate feedbacks. The uncertainty in modeling the processes involved in the carbon climate feedbacks therefore results in uncertainty in the predicted CO<sub>2</sub> concentration and hence

climate change. In the concentration-driven *piControl*, *historical*, and *rcp* experiments, however, the modeling uncertainty of these processes causes uncertainty in the diagnosed compatible anthropogenic CO<sub>2</sub> emissions, as discussed in section 6.

## 4. Climate Forcing Data for 1850–2100

[25] The forcing of the transient experiments from 1850 to 2005 and from 2006 to 2100 and further to 2300 follows in general the recommendations for CMIP5, as described below.

### 4.1. Earth Orbit

[26] The variation of the Earth orbit is modeled following the *Variations Séculaires des Orbites Planétaires* analytical solution by Bretagnon and Francou [1988], which is accurate for the years –4000 to +8000 for the epoch J2000.0.

### 4.2. Solar Irradiance

[27] The spectral solar irradiance at mean Sun-Earth distance is based on data provided by the SPARC/SOLARIS project (<http://sparsolaris.geomar.de/cmip5.php>). This irradiance is derived from observations and proxy data dating back to 1850, with annual resolution before 1882 and monthly resolution thereafter. The data include secular trends as well as the 11 year solar cycle and are scaled to measurements of the Total Irradiance Monitor (TIM), yielding a total solar irradiance of approximately 1361 W/m<sup>2</sup>. Spectral irradiance data for the RCP and ECP experiments consist of a repeated solar cycle 23 that begins in 1996 and ends in 2008, thereby keeping solar variability in the future comparable to that of the last years of the historical experiment. The spectrally resolved data are averaged over each of the 14 bands of the shortwave radiation scheme in ECHAM6 [Stevens *et al.*, 2013] and interpolated linearly in time.

### 4.3. Well-Mixed Greenhouse Gas Concentrations

[28] Concentrations of CO<sub>2</sub>, CH<sub>4</sub>, N<sub>2</sub>O, CFC-11, and CFC-12 are from the RCP database of the International Institute for Applied Systems Analysis (IIASA) (<http://www.iiasa.ac.at/web-apps/tnt/RcpDb>), for the historical period as well as for the scenarios. The annual mean concentrations are linearly interpolated to the middle of each month and provided as monthly constants to the radiation scheme. CH<sub>4</sub> and N<sub>2</sub>O decay with height in the stratosphere, with decay functions independent of time and geographical position. The transition heights of CH<sub>4</sub> and N<sub>2</sub>O to their mesospheric values are at 6.83 and 13.95 hPa, respectively. Mesospheric values are defined as a fraction of the tropospheric value. For details see Roeckner *et al.* [2003].

### 4.4. Anthropogenic CO<sub>2</sub> Emissions

[29] Anthropogenic CO<sub>2</sub> emission data are needed for the experiments *esmHistorical* and *esmrp85*, which follow on the unforced *esmControl* simulation. For *esmHistorical* (1850–2005), monthly CO<sub>2</sub> emissions from fossil fuel burning and cement production

(R. J. Andres, personal communication, 2011) are interpolated from a  $1^{\circ}$  grid to the model grid. Thereafter, emissions over ocean cells are relocated according to the models land sea mask to the next land grid point. Further, the monthly CO<sub>2</sub> emissions are converted to annual mean emissions. For *esmrcp85* (2006–2100), global emission values of the IIASA RCP database, which are specified in 10 year intervals, are linearly interpolated to each year and used to scale the annual mean emission pattern of the year 2005. The annual mean emissions are released homogeneously throughout the vertical extent of the atmospheric planetary boundary layer in *esmHistorical* and *esmrcp85*. Thus, the anthropogenic CO<sub>2</sub> emissions are constant during each calendar year.

#### 4.5. Ozone

[30] The ozone concentrations follow *Cionni et al.* [2011]. This data set merges three-dimensional tropospheric ozone concentrations from model simulations for the past and future with two-dimensional stratospheric ozone concentrations based on observations and scaling assumptions with respect to the emissions of ozone depleting substances in the past, and chemistry climate simulations for the future. The future tropospheric ozone was modeled separately for each RCP scenario, while the stratospheric ozone concentrations in all RCP scenarios originate from the same CCMVal-2 simulations, which were forced by the SRES A1B greenhouse gas scenario and the A1 adjusted halogen scenario [*Eyring et al.*, 2010]. These data were modified in two aspects for usage in MPI-ESM: First the original data, which extend upward only to 1 hPa, had to be extended vertically up to the highest model level at 0.01 hPa, and second the solar cycle signal, which is present only in the data of the past, had to be introduced to the data for the future to avoid a sudden change in the variability of the radiative forcing, especially in the middle atmosphere. These extensions are documented in *Schmidt et al.* [2012].

#### 4.6. Tropospheric Aerosols

[31] A global aerosol data set is used, describing past as well as future distributions of monthly and spectrally resolved aerosol optical properties (*Kinne et al.*, 2013). Central to this data set are the merged aerosol optical properties at 550 nm for year 2000 conditions, which are derived from the median of an ensemble of global models with advanced aerosol submodels and from ground-based sun-photometer observations from the AERONET network. The data set distinguishes coarse mode aerosols (radius  $> 0.5 \mu\text{m}$ ) of natural origin and fine mode aerosols containing an anthropogenic fraction. Only this anthropogenic fraction of the fine mode aerosols is varying over the years from 1850 to 2100. These variations are limited to the optical depth, while the vertical distribution and the composition are locally held constant. The evolution of the anthropogenic fraction from 1850 to 2005 is based on ECHAM5-HAM model simulations [*Stier et al.*, 2005]. The future distribution of the optical depth of anthropogenic aerosols is constructed as a linear superposition of the spatially resolved responses to standardized reductions in sulfur

emissions in 10 regions on the globe, multiplied with the time-dependent sulfur emissions in these regions. The response patterns for each of the 10 cases were obtained from ECHAM5-HAM simulations, for year 2000 conditions, in which the sulfur emission was reduced by 50% in each of these regions. Using this linearization and the regional emissions of the RCP scenarios, future global maps of anthropogenic fine mode aerosol optical depth were constructed for RCP2.6, RCP4.5, and RCP8.5, with the only restriction that the aerosol fine mode optical depth cannot become less than at preindustrial conditions. Beyond 2100, the anthropogenic aerosol optical depth is kept at year 2100 values.

#### 4.7. Stratospheric Aerosols

[32] Stratospheric aerosols are represented by their optical properties, which are provided for the historical period (G. Stenchikov, personal communication, 2010), extending the Pinatubo aerosol data set (PADS) of *Stenchikov et al.* [1998]. The data set describes zonal mean distributions of the extinction, single scattering albedo, and the asymmetry factor dependent on latitude, pressure and time, and spectrally resolved as needed by the ECHAM6 radiation scheme [*Schmidt et al.*, 2012]. For the *piControl* experiment, the idealized experiments *abrupt4xCO2* and *1pctCO2*, as well as for the scenario experiments *rcp26*, *rcp45*, and *rcp85*, the extinction by volcanic stratospheric aerosols is set to zero.

#### 4.8. Land Use Change

[33] In JSBACH, the anthropogenic land cover change is based on the New Hampshire Harmonized Land Use Protocol 3, which was developed by *Hurtt et al.* [2011] for CMIP5 in order to have a common data format for land use change in RCP scenarios. This protocol describes the anthropogenic land cover change in terms of land use transitions [*Hurtt et al.*, 2006], and vegetation cover is characterized using a classification only with respect to land use: two classes for natural vegetation (primary and secondary), and two classes of agricultural land cover (crops and pastures). For the implementation in JSBACH, however, primary and secondary natural vegetation are lumped together, as JSBACH does not include a description for current or past land use, e.g., in the form of wood harvest of natural vegetation. Thus, the actual data used from the Harmonized Protocol to drive JSBACH contain only transitions between natural vegetation (N), crops (C), and pasture (P). This coarse information on land use transitions is used to derive the more detailed information on land use transitions between the plant functional types of JSBACH, as described by *Reick et al.* [2013].

### 5. Climate and Climate Change in MPI-ESM

#### 5.1. Historical Simulations

[34] Because the *historical* experiment was not explicitly used during the tuning procedure of the MPI-ESM

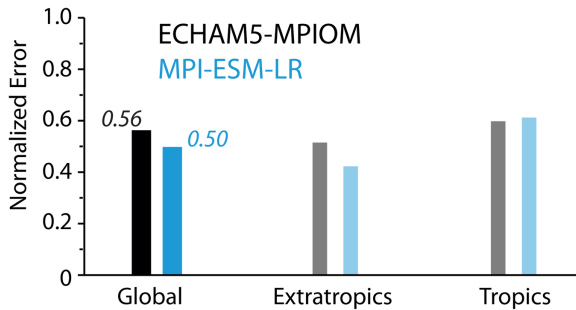


**Figure 2.** Modified Reichler-Kim standardized error based on variables summarized in Table 7 of Stevens and Bony [2012]. Lower is better and a value of one denotes the average of the CMIP3 coupled models.

[Mauritsen et al., 2012], it provides insights into the ability and the limitations of the model system to reproduce the general evolution of the observed climate, when driven by the assumed known external forcings. As the atmospheric general circulation model ECHAM6 alone has been used also with prescribed sea surface temperature and sea ice concentration boundary conditions, a comparison of the *historical* and *amip* simulations also provides some information on the systematic errors in the simulated climate of the recent past related to the atmosphere ocean coupling.

[35] Generally, the MPI-ESM model performance for the mean climate has improved compared to its predecessor ECHAM5/MPIOM (Figure 2), when quantified by the modified Reichler-Kim standardized error [Stevens and Bony, 2013, Table 7] and is 50% of the average standardized error of the CMIP3 models. The improvement compared to ECHAM5/MPIOM is mainly due to error reductions in the extratropics. In the following, the model performance for the mean climate shall be discussed for a few selected variables: temperature, precipitation, and ocean-heat content anomalies. For the variability performance, the Madden-Julian Oscillation and the El Niño/Southern Oscillation are briefly discussed. The simulation of the quasi-biennial oscillation in MPI-ESM-MR is discussed in Krismer et al. [2013].

### 5.1.1. Surface Temperature

[36] Figure 3 (top) presents the global and 12 month running mean surface air temperature change relative to the preindustrial period for MPI-ESM-LR (blue) and MPI-ESM-MR (red), and for the combined sea surface temperature and land surface air temperature records compiled by the Hadley Centre and the Climatic Research Unit in version 4.1 (HadCRU4.1) (black). For plotting purposes, the simulations and the CRU data are adjusted to have the same mean value during the period between 1961 and 1990. Figure 3 (middle) shows the shortwave forcing as measured by changes in the total absorbed solar irradiance at the top-of-atmosphere relative to a baseline value from the preindustrial simulation, indicating clearly the occurrence of the prescribed volcanic forcing. Figure 3 (bottom) shows the time series of the ocean heat content anomalies.

[37] Overall the simulations of both model configurations, MPI-ESM-LR and MPI-ESM-MR, reasonably reproduce the temperature signal of the 20th century in comparison to HadCRU4.1 data, despite a rather small aerosol forcing of  $-0.34 \text{ W/m}^2$  [Stevens and Bony, 2013]. Based on the general similarity of the LR and MR configurations of MPI-ESM found here for the evolution of the near surface temperature, only the LR configuration is discussed in the remainder of this paper. Despite the general ability of the models to simulate the evolution of the global mean near surface temperature, some notable deviations are observed between the model ensembles and the HadCRU4.1 data: (1) the midcentury warming is underestimated; (2) in the first decade of the 21st century, the simulations warm too rapidly; and (3) the model is consistently cooler than the observations during periods of volcanism. The deviation in the early 21st century is difficult to attribute to an adjusted forcing from the aerosol that is too small, because changes in the total aerosol loading over the past one or two decades have been small. The deviations in periods of volcanism suggest that either the volcanic forcing or the model response to the forcing is too strong. This strong negative surface air temperature response to volcanism likely compensates a tendency of the model to otherwise warm too much over the industrial period [Gregory et al., 2013].

[38] The zonal mean near surface land temperatures show biases of less than  $1^\circ$  in the tropics during all seasons, but pronounced warm biases in the northern midlatitudes and high latitudes during boreal winter and spring, and a cold bias in boreal summer [Hagemann et al., 2013, Figures 5 and 6]. The winter warm bias is most pronounced over eastern Siberia. The warm bias in the northern midlatitudes is even seen in the annual means. This bias is especially evident over the Eurasian Steppe in both the uncoupled amip (Figure 4a) and coupled historical simulations (Figure 4b). In general, the warm bias in the annual mean temperatures over the midlatitude grasslands is larger in the AMIP-type simulations—clearly revealed over North America. Over midlatitude mountain ranges a cold bias is evident, for instance over the Rocky Mountains, the Andes, and the Alps (Figures 4a and 4b). These cold biases over mountain regions seem to be more pronounced in the coupled model. In the coupled model (Figure 4b), large parts of the world oceans show deviations of less than one Kelvin [see also Jungclaus et al., 2013, Figure 2]. Like many coupled ocean-atmosphere general circulation models, the MPI-ESM has especially problems to simulate SSTs in the regions of the ocean gyres and in the upwelling regions west of the continents. Due to a too zonally oriented North Atlantic Current a cold bias occurs at the Atlantic subtropical gyre margins [Jungclaus et al., 2013]. Strong biases are also evident in the region of the Kuroshio Current. A rather strong warm bias is simulated in the upwelling region west of Africa—a quite common problem of coupled ocean-atmosphere models [see, e.g., Richter and Xie, 2008]. For a more detailed comparison and discussion of the simulated SSTs with observations, see Jungclaus et al. [2013].

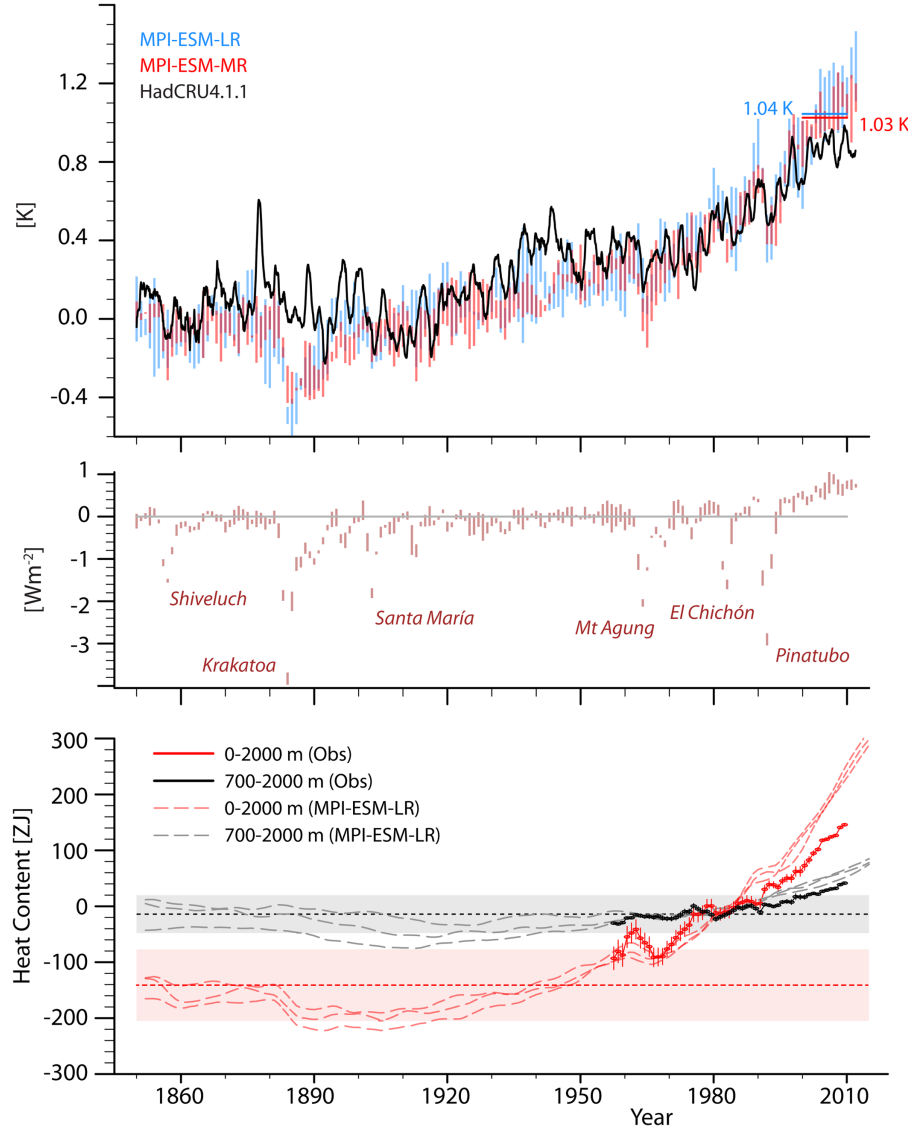


**Figure 3.** (top) Global mean surface air temperature change relative to the preindustrial period computed using the MPI-ESM-LR (blue) and MPI-EMS-MR (red) and compared to the HadCRU4.1 data (black curve, with 12 month running mean). For plotting purposes, the simulations and the CRU data are adjusted to have the same mean value during the period between 1961 and 1990. The colored bars span the range of annually averaged temperature deviations (from preindustrial) from an ensemble of three members for both the MR and LR configurations of the MPI-ESM. For the period after 1850 and 2005 the *historical* simulations were analyzed, for the period after 2005 the *rcp45* simulation was analyzed. (middle) Changes in short wave forcing associated with anthropogenic aerosols, volcanoes, and potential land surface or cloud changes as measured by changes in the total absorbed solar irradiance relative to a baseline value from the preindustrial simulation. Bars span the range of the MR and LR ensembles. (bottom) Time series of the world ocean heat content anomalies ( $10^{22}$  J) for the 0–2000 m (red) and 700–2000 m (black) layers based on 5 year running means. Reference period is 1955–2006. Solid lines depict observational estimates from Levitus *et al.* [2012] including their standard errors (vertical bars). Dashed lines represent the evolution in three realizations of the MPI-ESM-LR *historical* experiments. Horizontal dashed lines are the means and shadings indicate two-times standard deviations taken from the 1000 year unforced *piControl* simulation relative to the respective 1955–2006 ensemble means from the *historical* experiments.

### 5.1.2. Precipitation

[39] The largest precipitation biases occur over the tropical oceans. The uncoupled *amip* and coupled *historical* simulations show to first order a similar global oceanic precipitation bias pattern, but amplified in the

coupled *historical* simulations (Figures 4c and 4d). An exception is the warm-pool region of the tropical Pacific and the upwelling region of the tropical Atlantic sector. In the warm-pool area, a positive rainfall bias is simulated in the uncoupled simulations whereas in the

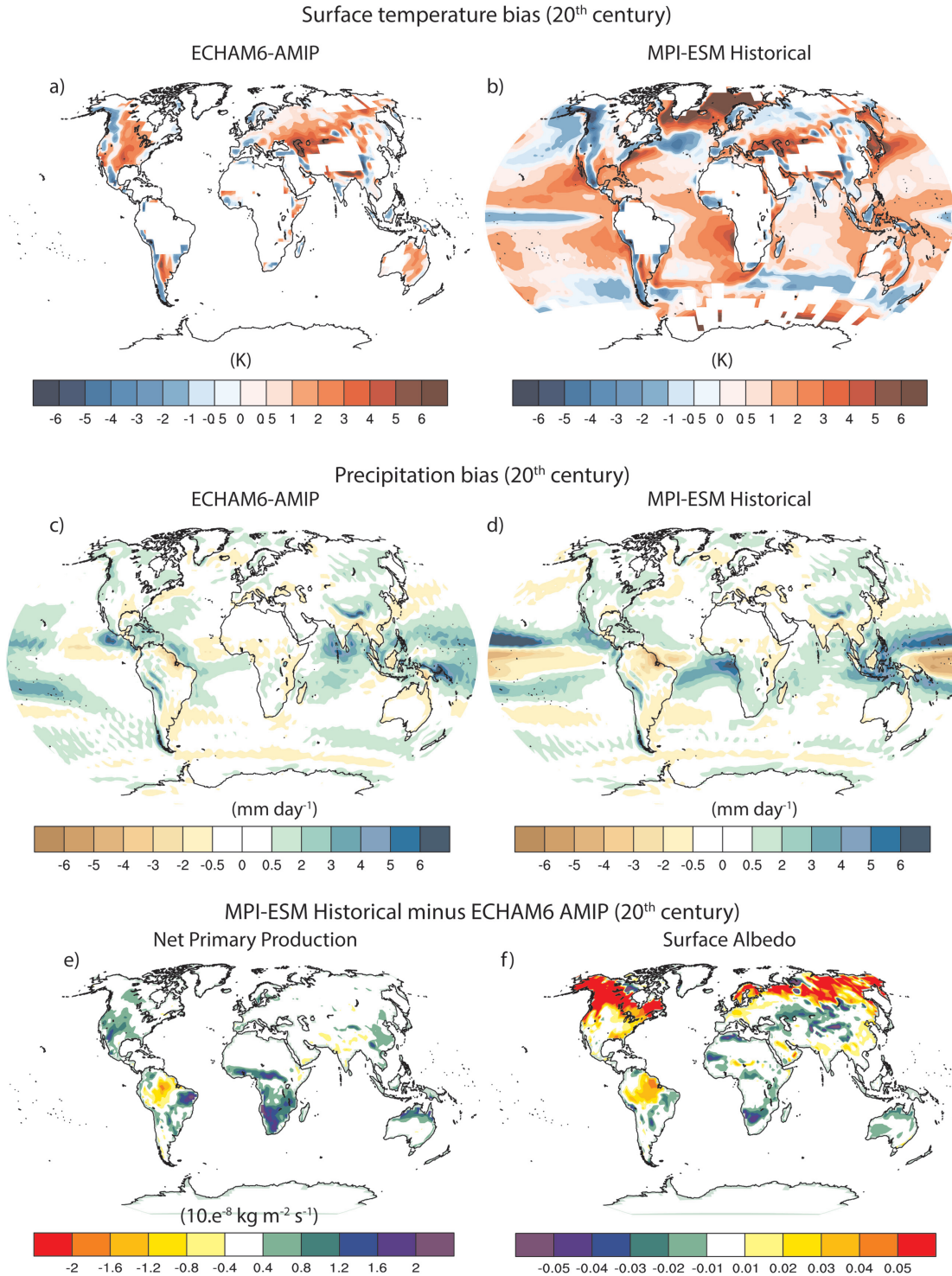


**Figure 4.** (top) Bias in surface temperature in (left) ECHAM6-AMIP and (right) MPI-ESM compared to HADCRU4 (1986–2005); (middle) bias in precipitation in (left) ECHAM6-AMIP and (right) MPI-ESM compared to GPCP (1986–2005); and (bottom) difference between MPI-ESM *historical* and ECHAM6 AMIP for 1986–2005: (left) Net primary production and (right) surface albedo.

coupled simulations a tripole-like bias pattern is seen. The strong wet tropical Atlantic Ocean bias in the coupled simulation is associated with a substantial

warm SST bias (Figures 4b and 4d). The oceanic ITCZ is shifted northward over the Pacific Ocean basin as well in the coupled as uncoupled model. The South

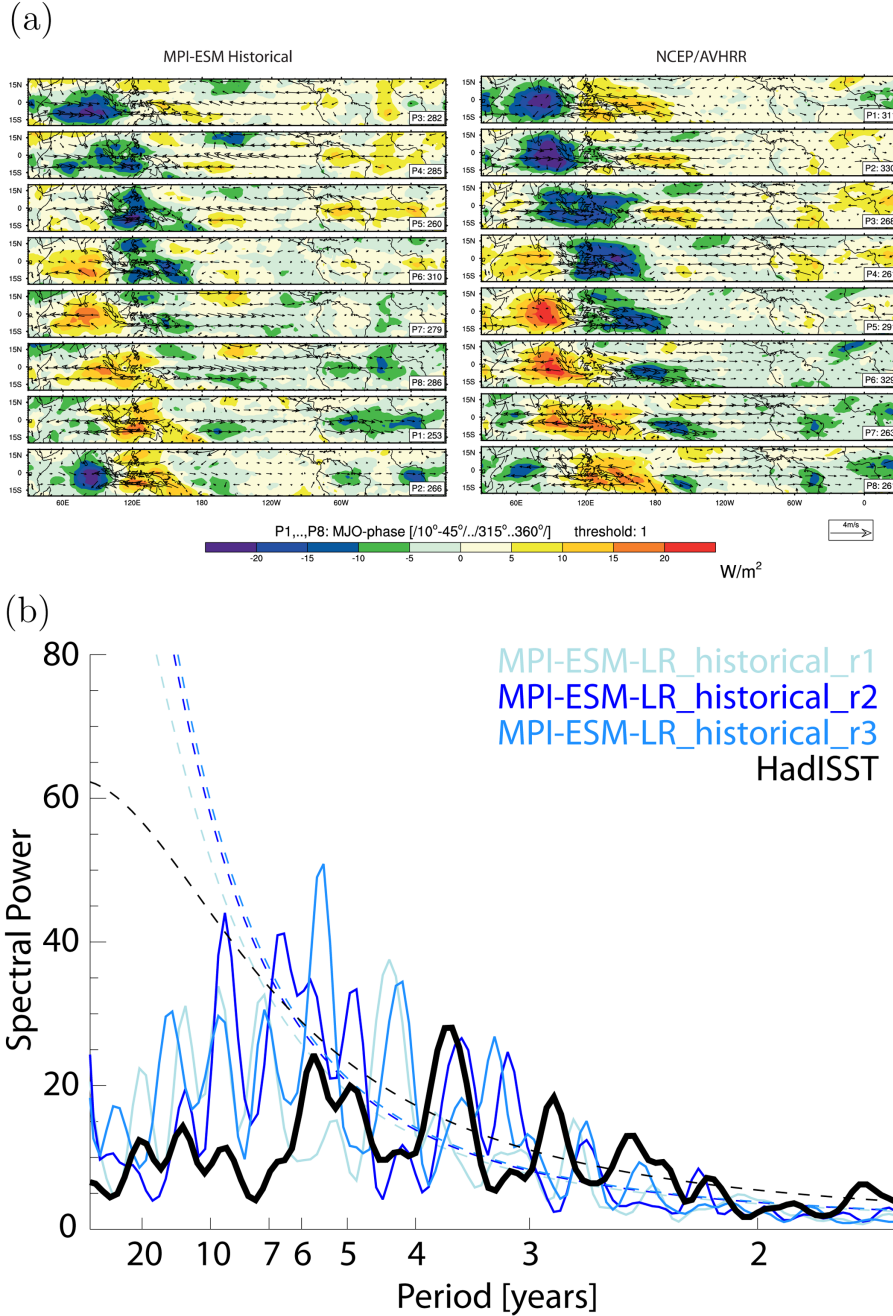


**Figure 5.** (a) Life cycle of the Madden-Julian Oscillation: Composite November to April 20–100 day filtered OLR (blue/green: enhanced convection; yellow/orange: suppressed convection) and 850 hPa wind anomalies (vectors) as a function of the MJO phase. (left) MPI-ESM Historical and (right) NCEP/AVHRR (1980–1999). (b) Variance spectra of monthly mean Niño3.4 SST anomalies (blue lines) from three ensemble members of the *historical* simulation (MPI-ESM-LR\_historical\_r1/2/3); thick black line indicates the respective spectrum from the HadISST data [Rayner et al., 2003]; the respective dashed lines indicate the 95% significance level of a corresponding AR1 process.

Pacific Convergence Zone is shifted equatorward. The *historical* MPI-ESM simulations capture the zonal distribution of land precipitation reasonably well during all seasons [Hagemann et al., 2013, Figure 3]. There exists a clear dry bias in the tropics north of the equator and in the subtropics over land. The model overestimates the precipitation along large orographic features

like the Andes, the Himalayas, and the Rocky Mountains (Figures 4c and 4d). These biases are largest in the boreal winter season [Hagemann et al., 2013] (Figure 4). Hot spots of precipitation biases are the regions of northeast Brazil (dry bias; see above) during boreal summer and eastern Asia (wet bias) in boreal winter. The dry bias over northeast Brazil is also visible in the

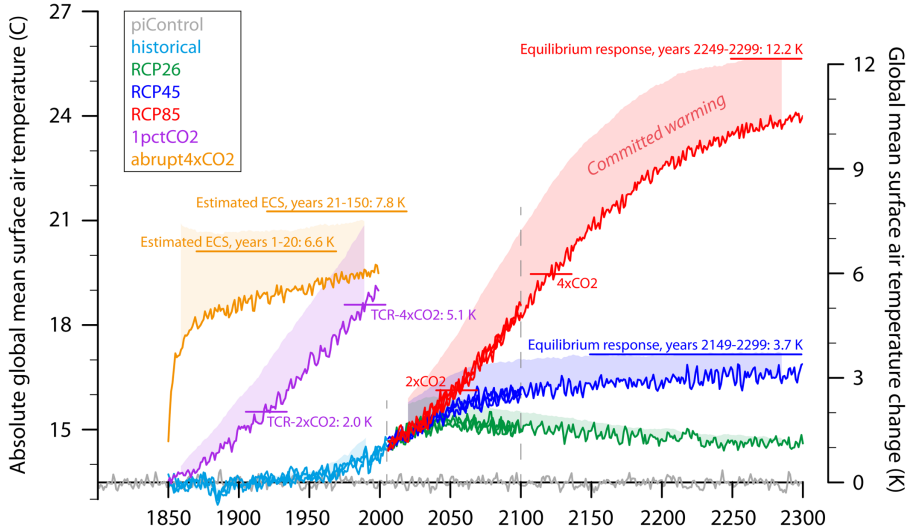


**Figure 6.** Overview of simulations performed with MPI-ESM-LR. Shown is annual mean globally averaged surface air temperature. Three realizations are shown for the *historical* experiment and for the RCP-projections up until 2100. Also shown are estimates of transient climate response at doubled and quadrupled CO<sub>2</sub> concentration in the *1pctCO<sub>2</sub>* simulation. Two regression-based estimates of equilibrium climate sensitivity are shown for the *abrupt4xCO<sub>2</sub>* experiment, and likewise for the *rcp45* and *rcp85* experiments based on regression during periods of constant forcing. Shaded areas are estimates of committed warming to be explained in the text.

annual means and clearly amplified in the coupled *historical* simulation compared to the *amip* simulation (Figures 4c and 4d).

### 5.1.3. Net Primary Production and Surface Albedo

[40] Figures 4e and 4f show differences between the uncoupled *amip* and the coupled *historical* simulations for the net primary production and the surface albedo, respectively, in contrast to Figures 4a–4d showing biases compared to observations.

[41] There are substantial differences in the net primary production in the tropical Atlantic sector between the coupled and uncoupled model version. These can be at least partly explained by the rainfall differences between the uncoupled and the coupled model. For example, the coupled *historical* simulation shows less rainfall over northeast Brazil than the uncoupled *amip* simulation (compare Figures 4c and 4d). This reduced rainfall is associated with a weaker net primary production over this area. Similar arguments hold for the southern African continent. These changes in the net primary production are impacting the surface albedo especially over these two regions. The reduced/enhanced primary production is associated with an enhanced/reduced surface albedo linking the biosphere in these regions to the physical world. It is evident that the largest surface albedo differences between the coupled and uncoupled simulations occur in the northern hemispheric polar regions, where the surface albedo is substantially higher in the coupled simulations.

### 5.1.4. Ocean Heat Uptake

[42] Observations and simulations show a substantial increase in ocean heat content since approximately the second half of the 20th century (Figure 3, bottom). The

simulated increase is clearly outside of the two-standard deviations of the preindustrial control simulation indicated by the respective shading. Therefore, the modeled ocean heat uptake cannot be explained without external forcing factors. Compared to the observational data [Levitus et al., 2012] MPI-ESM overestimates the ocean-heat uptake in recent decades substantially. By the end of the historical simulations in 2005, the simulated ensemble mean anomaly for the depth-range 0–2000 m is  $17.9 \pm 0.5 \times 10^{22}$  J, compared to  $12.0 \pm 0.3 \times 10^{22}$  J in the estimate by Levitus et al. [2012]. Note, however, that the range given for the observations does not include uncertainties due to applied methods, such as different interpolation and error correction. The simulated growth rates for the last 15 years are, for example, closer to the estimates given by Lyman et al. [2010] (not shown). On the other hand, an overestimation of ocean heat uptake appears to be a common feature in CMIP3 and CMIP5 models. Forest et al. [2008] and Kuhlbrodt and Gregory [2012] come to the conclusion that the models, including MPI-ESM, exaggerate vertical heat-transfer processes, probably due to generally weaker stratification. Comparing the simulated heat-uptake curves for the 0–2000 m and the 700–2000 m ranges, reveals that most of the mismatch between observations and simulations stems from the upper 700 m of the ocean. Similar to some of the CMIP3 models in Kuhlbrodt and Gregory's [2012] study (cf., their Figure 2c), the model overestimates warming in the upper 700 m while it reproduces the actual surface evolution relatively well (not shown). Comparing details of the regionally varying heat uptake in our model compared to observations is beyond the scope of this paper. Kuhlbrodt and Gregory [2012] points to the fact that one of

the key regions for ocean heat uptake is the midlatitude Southern Ocean, a region that is very sensitive to the choice of the eddy-diffusion parameterization [Kuhlbrodt and Gregory, 2012] and model resolution [Jungclaus *et al.*, 2013].

[43] The temporal variations in ocean-heat content apart from the global warming trend in the 20th century indicate the range of internal variability as expressed in the ensemble spread, but also the imprint of large volcanic eruptions. The simulations show a clear and persistent several decades long ocean cooling following the eruption of Krakatau in 1883 and preconditioning a relatively cold early 20th century [Gleckler *et al.*, 2006]. Reductions in ocean-heat content are also found after volcanic eruptions in the observational period. Here, the anomalies, for example, the reduction of the heat content after the Mount Agung eruption (1963), appear to be somewhat stronger in the observations compared to the model estimates.

### 5.1.5. Variability in the Coupled Historical Simulations

[44] We shortly discuss tropical modes of variability: The Madden-Julian-Oscillation (MJO) and the El Niño Southern Oscillation (ENSO) phenomenon. The MJO is the dominant mode of intraseasonal tropical variability [see Madden and Julian, 1971; Zhang, 2005]. ECHAM6 and MPI-ESM, as well as the predecessor models, have shown to simulate the MJO comparably well [Sperber *et al.*, 2005; Lin *et al.*, 2006; Sato *et al.*, 2009; Schubert *et al.*, 2013]. The MJO life cycle is often divided into eight phases [Waliser *et al.*, 2009; Crueger *et al.*, 2012]. Figure 5a shows these eight phases of the MJO life cycle for one ensemble member of the historical experiment (left) and the observed MJO (right) using NCEP reanalysis winds [Kalnay *et al.*, 1996] and AVHRR OLR [Liebmann and Smith, 1996]. The observations show suppressed and enhanced convection propagating eastward. Convective anomalies are strongest over the Indian Ocean, the Warm Pool, and the Western equatorial Pacific, minor signals are however also obvious in the Amazonian, Atlantic, and African areas. Accompanied with the changing convection patterns are anomalous westerlies and easterlies, obvious around the entire equatorial belt.

[45] The basic structure of the MJO is well simulated by the MPI-ESM-LR. The eastward propagating pattern of enhanced/suppressed convection and the accompanied wind anomalies are captured, as well as the decay of convection around the date line. However, the simulated MJO is less clearly structured and the convective anomalies are partly too weak and spatially too small.

[46] The ENSO representation has improved in terms of the amplitude compared to the predecessor model used in CMIP3. The Niño3.4 amplitude has decreased considerably from an overly strong  $1.26^{\circ}\text{C}$  in ECHAM5/MPIOM to  $0.75^{\circ}\text{C}$  that is close to the observed  $0.76^{\circ}\text{C}$ . The shape and amplitude of the ENSO power spectrum are relatively well simulated by the new model (Figure 5b). As in observations, the modeled ENSO exhibits a rather broad spectrum between 2.5 and 7 years. Two ensemble members of the

historical simulations show intensified power at decadal time scales compared to the observations (Figure 5b). While the reduction in amplitude makes the MPI-ESM simulations superior to earlier model versions, this does not hold for other ENSO-related characteristics, as discussed in Jungclaus *et al.* [2013]. The principal spatial ENSO pattern is simulated realistically. However, the more equatorially confined SST variability patterns stretch out further to the west compared to the observations. The model simulates much weaker teleconnections toward the central subtropical North and South Pacific and tropical western Pacific than observed. The teleconnection to the tropical Indian Ocean is slightly overestimated. The teleconnection to the Atlantic Ocean is reproduced relatively well and the reduced regression pattern amplitude in the Atlantic sector is another improvement over the ECHAM5/MPIOM model [cf. Jungclaus *et al.*, 2006] (Figure 13).

[47] In summary, the new MPI-ESM shows especially improvements in the extratropical mean state compared to its predecessor. No substantial progress is evident in the tropical mean climate. However, the model simulates satisfactorily the MJO and shows improvements in the simulation of the ENSO amplitude. The MPI-ESM shows pronounced deficiencies in its simulation of the tropical Atlantic climate. The model simulates a warm bias in the eastern tropical Atlantic impacting the zonal and meridional equatorial SST gradient. In the literature, the eastern tropical Atlantic SST error in coupled ocean-atmosphere models is linked to biases in the zonal winds associated with erroneous zonal precipitation over equatorial Brazil and Africa [Richter and Xie, 2008, Wahl *et al.*, 2011]. These precipitation biases are also seen in MPI-ESM with a pronounced dry bias in precipitation over northeast Brazil in summer (Figure 4d). In addition, the warm SST bias is likely related to a poor representation of marine boundary layer clouds in the atmospheric model [Stevens and Bony, 2013] as well as the sensitivity of the coupling between convective precipitation and the circulation [Möbis and Stevens, 2012]. In summer, the dry bias over northeast Brazil is even simulated when the atmospheric component of the MPI-ESM is forced with observed SSTs. This might indicate that deficiencies in the land surface conditions such as albedo and soil moisture might play a role. The largest part of the rainfall bias over northeast Brazil is induced by the coupling to the ocean leading to biases in simulated SSTs and associated moisture transports [Hagemann *et al.*, 2013]. As indicated by the literature, the biases in the tropical Atlantic region seem to be a coupled ocean-atmosphere-land problem. The understanding of tropical key processes—especially in the Atlantic sector—and their improvement in the model is ongoing work.

## 5.2. Estimates of Climate Sensitivity and Its Relation to Future Projections

[48] An overview of the global mean temperature evolution in the preindustrial control, historical, future projection and idealized experiments is given in Figure 6. In addition to the time evolution of the

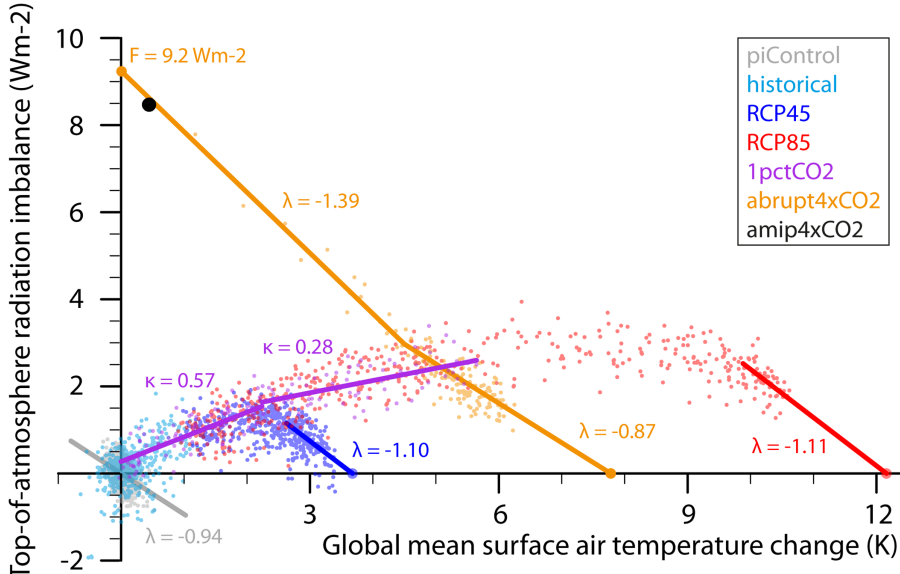


**Figure 7.** Gregory analysis of simulations with MPI-ESM-LR. For all experiments, regressions are done over periods with constant boundary conditions, except for the *1pctCO<sub>2</sub>* experiment where regressions are done over the periods of the first and the second doubling of CO<sub>2</sub>, respectively. A run with prescribed SSTs and quadrupled CO<sub>2</sub> is shown in black. Units of the slopes are [W m<sup>-2</sup> K<sup>-1</sup>].

temperature a number of diagnostics of transient and equilibrium climate sensitivity, as well as estimates of committed warming are presented, the rationale behind which we shall discuss in the next sections.

### 5.2.1. Forcing and Feedback-Analysis

[49] Coupled Model Intercomparison Projects previous to CMIP5 applied atmospheric models coupled to mixed-layer oceans to obtain estimates of equilibrium climate sensitivity to a doubling of CO<sub>2</sub>. Although these mixed-layer ocean models have the advantage that they can be run to equilibrium within a decade or so, not all institutes currently have the ability to run in this mode, and further it is sometimes being questioned whether, concerning climate sensitivity, these models are representative of their fully coupled models. Therefore, it was decided to instead use the fully coupled ESMs and to apply a framework for interpreting the evolution of a climate system out of balance with a constant forcing [Gregory *et al.*, 2004]. Here, the global mean surface temperature change ( $\Delta T$ ) is related to the top-of-atmosphere radiation imbalance ( $\Delta R$ ) through the adjusted forcing ( $F$ ) and effective feedback factor  $\lambda$ :

$$\Delta R = F + \lambda \cdot \Delta T \quad (1)$$

[50] By linearly regressing  $\Delta R$  on  $\Delta T$  in an experiment with an abruptly increased forcing it is possible to infer  $F$  as the  $y$  intercept and  $\lambda$  as the slope of the line. By assuming  $\lambda$  remains the same at all times also equilibrium climate sensitivity (ECS) can be estimated as the intersection with the  $x$  axis, where  $\Delta R = 0$ . If the system is linear one can also estimate ECS from the coefficients as  $ECS = -F/\lambda$ . Note that in CMIP5, because the fully coupled models typically exhibit substantial internal variability, it was decided to double the forcing relative to

earlier by abruptly quadrupling instead of doubling the atmospheric CO<sub>2</sub> concentration, in order to obtain a better signal-to-noise ratio. Hence, one must divide by two for the estimates of forcing and equilibrium climate sensitivity to be comparable to a single doubling of CO<sub>2</sub>.

[51] For MPI-ESM-LR—as is the case for a number of other coupled models [Andrews *et al.*, 2012]—the linear approximation does not hold well for the entire *abrupt4xCO<sub>2</sub>* run (Figure 7). Instead, for this model it has been previously suggested to somewhat arbitrarily divide the run in two piecewise nearly linear portions of the first 20 years and the last 130 years of the simulation [Stevens and Bony, 2013; Block and Mauritsen, 2013]. Clearly, the total feedback factor is different between the regressions (Figure 7), and so also the resulting estimated ECS depend upon which period is used. Using the linear regressions of the first 20 and last 130 years, the estimates for the ECS is 6.6 or 7.8 K (Figure 7). Using a single linear regression for the whole period yields an ECS value of 7.3 K, as in Andrews *et al.* [2012], which is naturally between our two estimates. But it should be noted that the extrapolation to  $\Delta R = 0$  explicitly assumes that the total feedback factor remains unchanged until the full equilibration of the experiment. In a recent study, Li *et al.* [2012] integrated the predecessor ECHAM5/MPIOM coupled model at coarse resolution to equilibrium. They found a regime between years 1200 and 6000 where global mean temperature changes relatively little as the system relaxes further toward equilibrium, equivalent of a large negative  $\lambda$ . Whether this effect occurs in the *abrupt4xCO<sub>2</sub>* experiment, if continued, has not been tested.

[52] The underlying cause of the distinct nonlinearity of the feedback factor found in MPI-ESM-LR as well as several other coupled models is a topic of ongoing

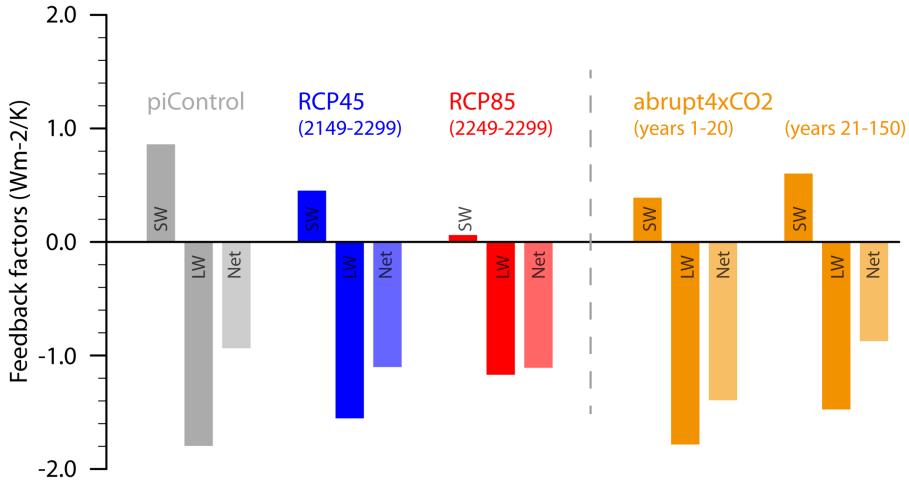


**Figure 8.** Feedback factors from different simulations broken into longwave and shortwave components. Units are  $[W\ m^{-2}\ K^{-1}]$ .

debate. Possible explanations include decadal time scale adjustments of the ocean circulation, differential warming patterns for example associated with ocean heat uptake, or state dependencies of the radiative feedback factors [Senior and Mitchell, 2000; Winton et al., 2010; Block and Mauritsen, 2013]. Although many models exhibit the same behavior in terms of their global feedback, it remains an open question to which extent the underlying cause is robust across models. For example, Senior and Mitchell [2000] found that in the HadCM2 model the slower warming of the Southern Ocean induced cloud feedback supported the change in feedback, whereas Block and Mauritsen [2013] found feedback in the Southern Ocean to oppose the increasing climate sensitivity in MPI-ESM-LR.

[53] The choice to divide the *abrupt4xCO<sub>2</sub>* run into two pieces is, however, supported by an AMIP simulation with prescribed SST, but quadrupled CO<sub>2</sub> relative to the standard AMIP simulation (Figure 7, black symbol). Because land-surface temperatures are not held fixed the global mean  $\Delta T$  is slightly positive. The mean over the 30 year *amip4xCO<sub>2</sub>* simulation aligns well with the regression line from the first 20 years of the *abrupt4xCO<sub>2</sub>* simulation. The resulting adjusted forcing is 9.2  $W\ m^{-2}$ , which is substantially larger than twice the radiative forcing of 3.7  $W\ m^{-2}$  that is typically reported for a single doubling of CO<sub>2</sub> after stratospheric adjustment [e.g., Stuber et al., 2001]. The reason for the discrepant CO<sub>2</sub> forcing estimates is a fast cloud adjustment of about 2  $W\ m^{-2}$ , in MPI-ESM-LR primarily due to a cloud reduction in direct response to the quadrupled CO<sub>2</sub> [Block and Mauritsen, 2013].

### 5.2.2. Feedback Analysis LW/SW

[54] In addition to the *abrupt4xCO<sub>2</sub>* experiment, also the extended *rcp45* and *rcp85*, as well as the *piControl* simulations offer periods with constant forcing allowing to estimate  $\lambda$  by linear regression (Figure 7). The extended scenarios indicate feedback factors in good agreement with each other (*rcp45*:  $\lambda = -1.10$ , *rcp85*:  $\lambda = -1.11$ ), and in between the two estimates from

*abrupt4xCO<sub>2</sub>* ( $\lambda_{1-20} = -1.39$  and  $\lambda_{21-150} = -0.87$ ). The total feedback factor obtained from *piControl* is relatively weak ( $\lambda = -0.94$ ); possibly indicating that internal variability in the model is less damped than externally forced climate change. It should be noted that only the last 50 years of *rcp85* can be used, and because the temperature change during this period is relatively small the estimate is associated with considerable uncertainty.

[55] Whereas the total feedback factor changes only from  $-0.94$  to  $-1.1$  between the *piControl*, *rcp45*, and *rcp85* simulations, the shortwave component exhibits a substantial weakening in the warmer climates, reducing from 0.8 in *piControl* to 0.1 or almost zero in *rcp85*. A weakening of similar size is observed in the longwave component that changes from  $-1.8$  to  $-1.1$ , such as to nearly compensate each other (Figure 8). The near-zero shortwave feedback in the *rcp85* simulation is likely explained by the disappearance of sea ice at temperatures about 7 K above preindustrial [Notz et al., 2013].

[56] In *abrupt4xCO<sub>2</sub>*, the longwave feedback also weakens in the warmer part of the simulation, explaining about half the positive change in the total feedback factor, whereas the shortwave feedbacks strengthen in the warmer part and thus contribute to the increase in climate sensitivity. This is consistent with a strengthening of the longwave water vapor and cloud feedbacks, and a delayed sea ice melt in the *abrupt4xCO<sub>2</sub>* simulation [Block and Mauritsen, 2013].

### 5.2.3. Transient Climate Response and Committed Warming

[57] A different perspective to climate sensitivity is provided by idealized experiments where the forcing is ramped up at a constant rate every year as is done in the *IpcrCO<sub>2</sub>* experiment. Here, the underlying assumption is that the radiative forcing is logarithmic in the atmospheric CO<sub>2</sub> concentration [Arrhenius, 1896]. The transient climate response (TCR) is defined as the temperature change by the time CO<sub>2</sub> has been doubled (every 70 years). Interestingly, also this idealized

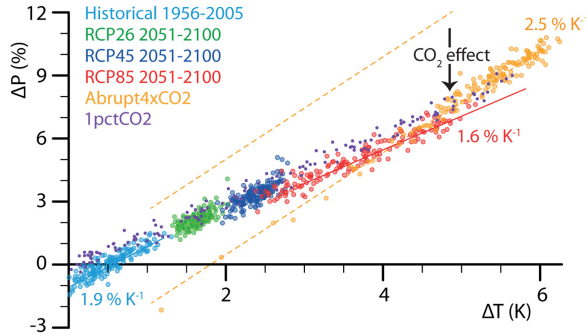


**Figure 9.** Changes in globally averaged precipitation versus changes in globally averaged surface air temperatures. Changes are measured against the preindustrial control simulation. Differences in precipitation are measured relatively, in percent.

experiment exhibits considerable nonlinearity, with the first doubling of CO<sub>2</sub> yielding a TCR of 2.0 K, and the second doubling from 2 × CO<sub>2</sub> to 4 × CO<sub>2</sub> a higher TCR of 3.1 K (Figure 6). A similar qualitative behavior is found in the *rcp85* experiment with stronger transient warming during the second doubling of CO<sub>2</sub>, although a direct comparison is hampered by the fact that other forcing agents are at play. The reason for the increase in TCR for MPI-ESM-LR must be sought in a considerable weakening of the ocean heat uptake efficiency  $\kappa$ , defined as the regression between  $\Delta R$  and  $\Delta T$  in the *1pctCO2* simulation (Figure 7). In the earlier part of the simulation, a larger fraction of the energy goes into the oceans, hence  $\kappa$  is large, leading to weaker transient surface warming relative to the warmer part of the simulation. A plausible explanation is that the stabilization of the oceans naturally occurring when warming from above makes it increasingly difficult to transfer heat to the deep oceans [Watanabe et al., 2013].

[58] The forced experiments, be it the idealized or the future projections, have not reached equilibrium with respect to the applied forcing within the duration of the experiments. Due to the large heat capacity and long time scales inherent to ocean heat uptake it takes essentially thousands of years to reach the climatic equilibrium response [Li et al., 2012]. One can estimate this warming still “in the pipeline” [Hansen et al., 2011] by defining a committed warming ( $\Delta T_c$ ), which is the equilibrium response to the forcing applied at any instance during a transient run:

$$\Delta T_c = \Delta T - \Delta R/\lambda, \quad (2)$$

where it is assumed that the feedback factor  $\lambda$  is a known constant, and  $\Delta R$  and  $\Delta T$  are the transient global mean temperature and radiation imbalance. One can think of the estimated committed warming as the temperature change that would be attained after a long time if all the greenhouse gases would be held constant at the current level. We visualize the committed warming in Figure 6 as shaded areas, calculated by assuming  $\lambda = -1.1 \text{ W m}^{-2} \text{ K}^{-1}$  and applying a 20 year running

mean to the time series of  $\Delta T$  and  $\Delta R$ . The committed warming changes when the forcing evolves and stays nearly constant during periods of constant forcing, such as the periods at the ends of the extended *rcp45* and *rcp85* simulations used for the Gregory analysis. Also the committed warming in the idealized experiments behave as expected with  $\Delta T_c$  in the *1pctCO2* experiment nearly reaching the level of  $\Delta T_c$  in *abrupt4xCO2* by the time of quadrupling CO<sub>2</sub>. At times the committed warming can be substantially different from the transient response, for example the committed warming in the *rcp85* simulations exceeds the realized warming by more than 2 K by the end of the 21st century.

#### 5.2.4. Precipitation Sensitivity

[59] Precipitation changes are influenced both by the warming, and by changes in atmospheric CO<sub>2</sub> [Mitchell et al., 1987; Allen and Ingram, 2002; Bony et al., 2013]. Changes in radiative fluxes attributed to CO<sub>2</sub> alone reduce the rate at which the troposphere cools, which is associated with a reduction in globally averaged precipitation. However, the warming that eventually occurs after the addition of CO<sub>2</sub> to the atmosphere, and associated changes in the absolute humidity, lead to a marked increase in the rate at which the troposphere cools [Mitchell et al., 1987; Stevens and Bony, 2013]. For the CMIP3 models analyzed by Lambert and Webb [2008], global precipitation varied with warming by 1.4–3.4% K<sup>-1</sup>: By regressing global precipitation changes against surface air temperature changes taken from the *abrupt4xCO2* simulation of MPI-ESM-LR (Figure 9), a precipitation sensitivity in the middle of this range, 2.5% K<sup>-1</sup> is found. A similar regression performed for the scenarios run by MPI-ESM-LR result in a much smaller sensitivity, of about 1.9% K<sup>-1</sup> for the weakly forced scenarios (*rcp26* or *rcp45* or the later part of *historical*), and 1.6% K<sup>-1</sup> toward the later part of the 21st century for the *rcp85* scenario (Figure 9), which is very similar to the sensitivity found for *1pctCO2*. These differences between the precipitation sensitivity of simulations with an abrupt change in CO<sub>2</sub>—as compared to simulations forced by a secular trend in CO<sub>2</sub>—can be understood as a simple consequence of the direct effect of CO<sub>2</sub> on atmospheric heating, which tends to reduce precipitation. Additionally, for more extreme warming the lower atmosphere will become optically thick, which will reduce the precipitation sensitivity [e.g., O’Gorman and Schneider, 2008].

#### 5.3. Regional Response Patterns

[60] The regional patterns of changes in near surface temperature and precipitation from the 1850 climatology of *piControl* to the late 20th century in the historical simulation and from the late 20th to the late 21st century in the three RCP scenarios are displayed in Figure 10. Temperature change patterns for both time periods and for all three scenarios exhibit the largest warming in the Arctic, generally more warming over land than over ocean and the least warming in the Southern oceans and in the North Atlantic. The amplitude of the warming in the 21st century depends strongly on the

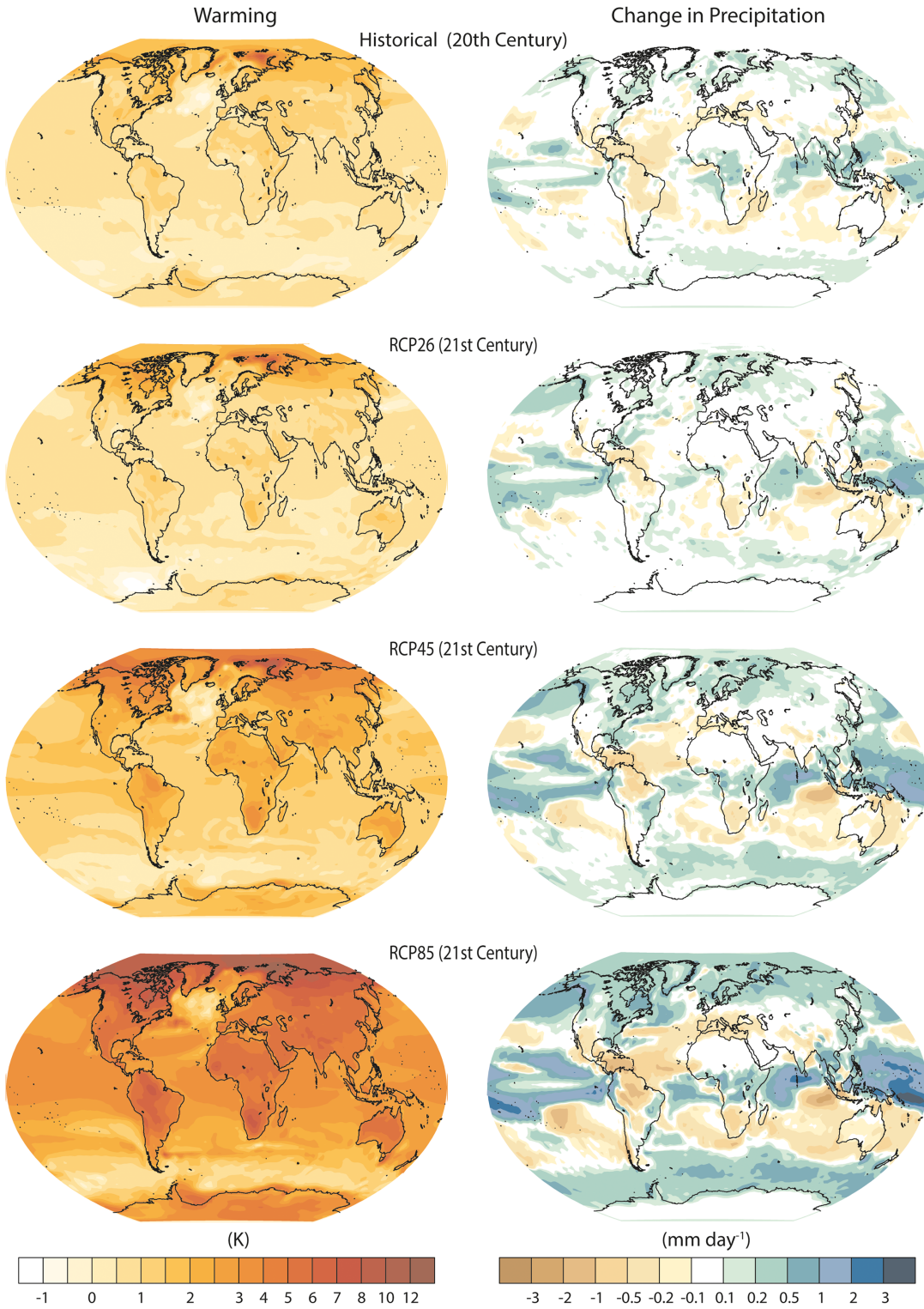


**Figure 10.** Change of annual mean near surface (left) temperature and (right) precipitation. *Historical* 20th century (1986–2005) compared with 1000 year *piControl* (first panel); RCP 21st century (2081–2100) compared with *historical* (1986–2005): *rcp26* (second panel), *rcp45* (third panel), and *rcp85* (fourth panel).

scenario. In *rcp85*, this warming exceeds 10 K in most of the Arctic, while it remains at or below 3 K in *rcp26*. However, the warming patterns of the three RCP simulations have a high similarity, if normalized by the global

mean warming (Figure 11, left). In other words, in MPI-ESM, the local amplification factor with respect to the global mean warming is largely robust across the range of scenarios used here.

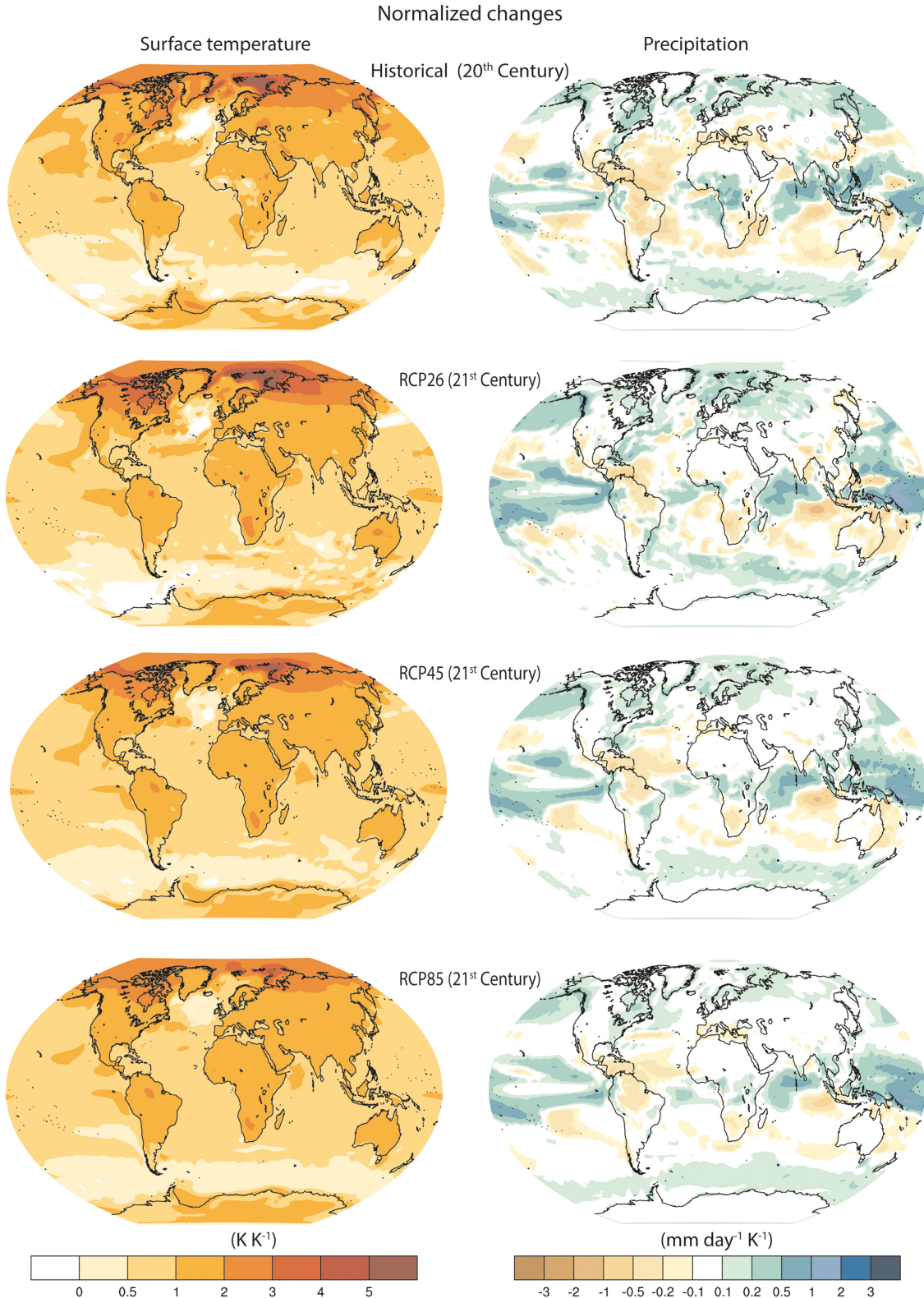


**Figure 11.** As Figure 10, but scaled by the change in global and annual mean near surface temperature.

[61] The degree of Arctic amplification in MPI-ESM-LR is in the midrange of the CMIP5 ensemble (Figure 12) and of estimates derived from CMIP2 [Holland and Bitz, 2003] and CMIP3 models [Winton, 2006]. There

are slight differences among the scenarios, with more strongly forced scenarios showing a tendency toward less Arctic amplification. This is most evident in the zonal mean amplification factor north of 50°N (Figure

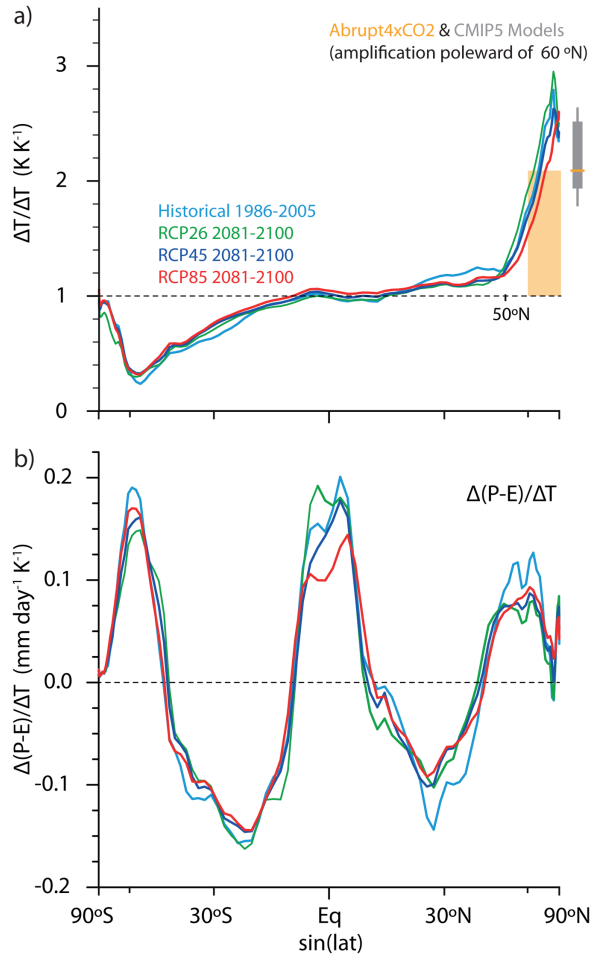


**Figure 12.** Changes in zonally averaged climate: (a) temperature amplification factors; (b) changes in precipitation minus evaporation. Temperature amplification factors are defined as the change of the zonally averaged temperature versus the global average temperature change. The global average of the temperature amplification factor is unity by definition, and the global average of the difference between precipitation and evaporation is likewise zero. The gray box for CMIP5 shows the ensemble mean  $\pm$  standard deviation of Arctic amplification (of surface temperature change north of  $60^{\circ}\text{N}$ ), whiskers denote the full spread.

12a). At the same time, the latitude of maximum warming is displaced poleward. This is consistent with the latitude of maximum warming being closely related to the retreating sea ice edge [Holland and Bitz, 2003]. The *abrupt4xCO<sub>2</sub>* simulation shows a similar Arctic amplification as *rcp85*. For *abrupt4xCO<sub>2</sub>*, the deviation of the amplification factor from unity for the warming of the last 50 years of the simulation is displayed in Figure 13. As discussed for the warming of the RCP simulations, the amplification factor shows the largest positive deviations in the Arctic, followed by the continents, and the largest negative deviations over the oceans in the southern latitudes and in the North Atlantic.

[62] Patterns of annual mean precipitation change are displayed in Figure 10 (right). For both periods and all scenarios, the precipitation increases primarily in equatorial and in higher latitudes, with typically higher changes over ocean surfaces. Precipitation decreases are found in the subtropics of both hemispheres. Overall, wet latitudes get wetter and dry latitudes get drier. A particular feature is the reduction in precipitation that extends from South America across the tropical Atlantic to the Mediterranean. Between the three scenarios the warmest exposes the strongest precipitation changes, as expected. The differences in strength are to a large extent explained by the global warming, as seen in the scaled patterns (Figure 11, right), though minor systematic differences exist in the tropics, as seen in the zonal mean changes of precipitation minus evaporation (Figure 12b). Here the increase in precipitation is less marked for the more strongly forced simulation. This pattern of response is consistent with a slowdown in the tropical overturning circulation associated with the radiative effects of CO<sub>2</sub> [Bony et al., 2013]. Analysis of the full spatial pattern of the response shows the biggest difference in the tropics centered over the tropical western Pacific and eastern Indian Ocean, where precipitation itself maximizes. This pattern is also consistent with a weakening Walker circulation. In the midlatitudes and high latitudes, there is some evidence that the more strongly forced simulations increase their precipitation proportionally more than do the weakly forced simulations (compare *rcp85* to *rcp26* at  $60^{\circ}\text{N}$ ). These differences cannot be explained by the normalization based on globally, instead of locally or latitudinally, averaged temperatures, which would be more relevant to the thermodynamic arguments that explain the pattern of precipitation changes in Figure 12b [Mitchell et al., 1987; Held and Soden, 2006].

[63] The historical simulation differs in its pattern of response from the more weakly forced scenario (which has the most similar global temperature change), particularly in the storm-track regions. Here, the increase in the precipitation in the historical simulations is proportionally (20%) greater than in the scenarios in both hemispheres (Figure 12b). This change is balanced by commensurately larger drying in the subtropics. These changes are not well understood, but indicative of a stronger poleward flux of moisture per unit of temperature change in the late historical period compared to future projections. Overall, the analysis shows the powerful influence of the globally averaged temperature change in scaling response patterns that are otherwise similar across a wide range of scenarios. It also suggests that given the precision of the global modeling, the added value of additional scenarios may be rather limited.

## 6. Carbon Cycle in MPI-ESM

### 6.1. Calibration and Equilibration of the Carbon Cycle

[64] A major task in preparing the CMIP5 simulations was to set up the MPI-ESM carbon cycle such

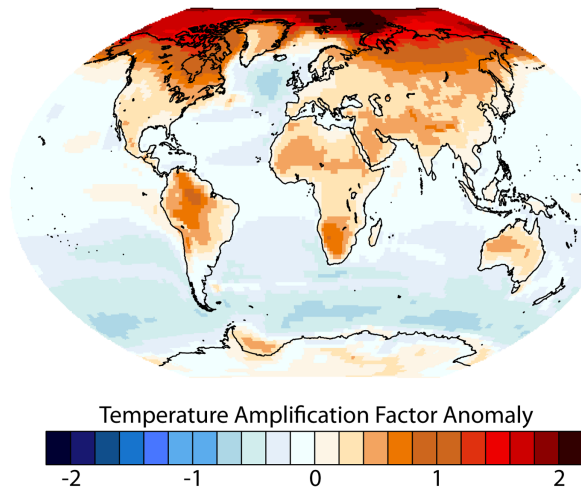


**Figure 13.** Normalized deviation from global mean warming ( $\Delta T / \Delta T_{\text{global}} - 1$ ) from years 100–150 of *abrupt4xCO<sub>2</sub>*, positive/negative values indicating more/less warming than the global average.

that it is in equilibrium for preindustrial conditions and reproduces in historical simulations observed conditions. To this end, in a first step biogeochemical land and ocean processes were tackled separately.

[65] Considering first ocean biogeochemistry, HAMOCC was integrated for several thousand years driven by climatological forcing and a preindustrial atmospheric pCO<sub>2</sub> of 278 ppmv until an equilibrium state was obtained for the ocean biogeochemistry. This state was then taken as initial state for the ocean biogeochemistry in a full MPI-ESM-LR preindustrial spin-up simulation, lasting about 1000 years using a fixed atmospheric CO<sub>2</sub> concentration and a fixed vegetation distribution. To keep the overall carbon and silica content of the system constant, losses to the sediment were compensated by a globally uniform input of silicate, alkalinity, and dissolved inorganic carbon to the ocean, see *Ilyina et al.* [2013] for details.

[66] In parallel, the land carbon cycle was adjusted. To bring the land carbon pools to equilibrium, the JSBACH carbon pool scheme was integrated for several thousand years using leaf area index, net primary productivity, soil temperature, and soil moisture data from the above mentioned coupled preindustrial MPI-ESM-LR spin-up simulation. The resulting land carbon pool state was then used in a second preindustrial spin-up simulation with MPI-ESM-LR, but now with interactively varying geographic distribution of vegetation as simulated by the dynamic vegetation component of JSBACH [*Reick et al.*, 2013]. By this simulation, not only was the land carbon cycle further equilibrated, but a climate-consistent vegetation distribution was also obtained. This simulation was performed with an accelerated vegetation dynamics to reach equilibrium of the vegetation distribution already after a few hundred years. The analysis of this spin-up simulation confirmed that the overall physical state was largely unaffected by shifts in vegetation distribution.

[67] Next, the state of the whole land surface at the end of the second MPI-ESM-LR spin-up simulation was combined with the state of the atmosphere, ocean, and ocean biogeochemistry from the first MPI-ESM-LR simulation to start a final spin-up run lasting 900 years including vegetation dynamics.

[68] Finally, a historical test simulation was performed, starting from the final preindustrial spin-up state to estimate the net land carbon uptake since 1850. Based on these results, the parameter for the fraction of living carbon directly emitted to the atmosphere during a land use transition was adjusted such that the historically accumulated net carbon uptake by land fits observation-based estimates for 1800–1994 (*Sabine et al.* [2004]:  $39 \pm 28$  GtC; *Matsumoto and Gruber* [2005]:  $31 \pm 28$  GtC). Since this parameter has no effect on the preindustrial equilibrium state, the final state of the last spin-up simulation could then be taken as the initial state for the *piControl* simulation. The final result of this calibration is shown in Figure 14: the three realizations of the *historical* and *esmHistorical* simulations give between 1850 and 1994 a carbon uptake between 14.2 and  $-1.6$  GtC, compatible with the above values. In our simulations, land loses carbon until the 1960s by deforestation. At this point increased plant carbon uptake due to CO<sub>2</sub> fertilization overrules carbon losses from agricultural expansion. However, according to a recent observation-based study by *Huang and Elroy* [2012] this switch from source to sink should already happen in the 1940s.

[69] The final preindustrial spin-up state of MPI-ESM-LR was used as basis for the MPI-ESM-MR spin-up. As in the latter, the land component is identical to the low-resolution MPI-ESM-LR we interpolated only the oceanic fields onto the high-resolution ocean grid and performed a several hundred years long spin-up run with the full system, see details in *Jungclaus et al.* [2013] and *Ilyina et al.* [2013].

## 6.2. Atmospheric CO<sub>2</sub>

[70] A direct impression of the performance of the carbon cycle in MPI-ESM-LR can be obtained by comparing observation data on atmospheric CO<sub>2</sub> concentration with simulation results from the *esmHistorical* simulation, where atmospheric CO<sub>2</sub> is a prognostic variable (Figure 15). Overall, the historic increase of atmospheric CO<sub>2</sub> is well reproduced by the model as seen from the comparison with reconstructions of the CO<sub>2</sub> concentration from Antarctic ice cores. The stalling in CO<sub>2</sub> increase during the 1940s suggested by ice core data, however, is not captured in the simulations, and from this point on the slope of the simulated CO<sub>2</sub> increase is a bit weaker than observed until it almost exactly merges with the observed values in 2005. For several stations, worldwide continuous CO<sub>2</sub> measurements are available that reflect the seasonal cycle of CO<sub>2</sub>. For the atmospheric CO<sub>2</sub> concentration at Mauna Loa measured and simulated amplitude and phase of the seasonal cycle nicely match (see large inset in Figure 15). However, at other stations from the international CO<sub>2</sub> sampling network the seasonal amplitude is

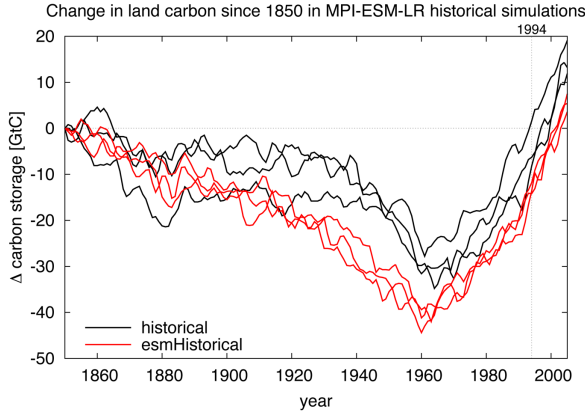


**Figure 14.** Change in land carbon since 1850 in the three realizations of the *historical* and *esmHistorical* simulations with MPI-ESM-LR.

overestimated in the model simulation which is most likely the consequence of an overestimation of net primary productivity in ocean and land biology of MPI-

ESM in combination with uncertainties in atmospheric tracer transport. This overestimation is particularly severe in the southern hemisphere, as seen for instance in the comparison with the South Pole flask data (see small inset in Figure 15), but is less expressed in the northern hemisphere.

### 6.3. Ocean Carbon Uptake

[71] The World Ocean is capable of taking up and storing large amounts of CO<sub>2</sub> from the atmosphere [e.g., Maier-Reimer and Hasselmann, 1987; Sabine et al., 2004] and has already taken up about 1/3 of anthropogenic CO<sub>2</sub> emitted since the onset of industrial revolution [Le Quéré et al., 2009]. Despite its function as carbon reservoir, certain areas of the ocean act as net sinks or net sources of CO<sub>2</sub> over the year [Key et al., 2004]. These geographic patterns in the air-to-sea CO<sub>2</sub> flux, resulting from a combination of physical, chemical, and biological properties together with hydrodynamic conditions, are well captured in MPI-ESM simulations within CMIP5 [Ilyina et al., 2013]. For instance, colder waters can dissolve more gaseous CO<sub>2</sub> than warmer

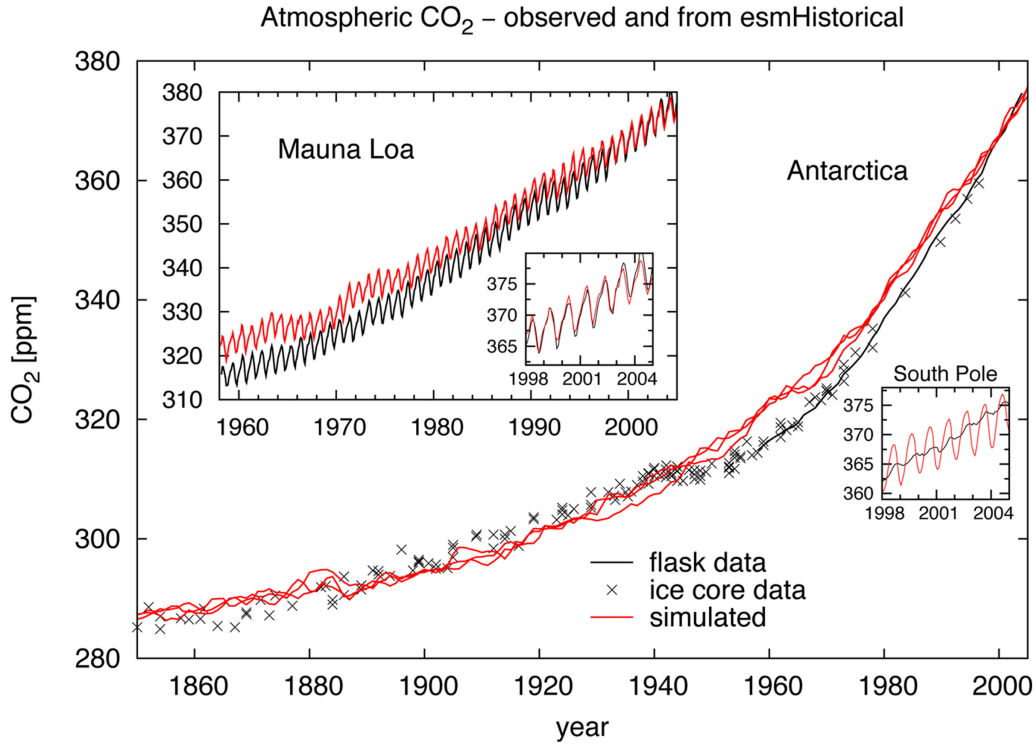


**Figure 15.** Atmospheric CO<sub>2</sub> simulated in *esmHistorical* as compared to observations. The large figure refers to the annual mean CO<sub>2</sub> time series over Antarctica, whereas the smaller inset figures show the monthly mean CO<sub>2</sub> time series at Mauna Loa and at the South Pole. Simulation data are shown as solid red lines. For Antarctica data from all three realizations are shown, whereas the inset figures are based on monthly mean data of the first realization only. Simulation data for Antarctica are taken from the grid box centered at (335.625°E, 88.572°S) at 600 hPa. The results for Mauna Loa are from the grid box centered at (204.375°E, 19.585°N) at 600 hPa. These grid boxes cover the locations where the flask sampling data shown in the figure are taken. Observational data are shown in black: black solid lines indicate flask and in situ measurements of CO<sub>2</sub>, whereas ice core reconstruction data are shown as crosses. Data origin: Ice core reconstructions are from Law Dome [Etheridge et al., 1996; MacFarling et al., 2006] and WAIS [Ahn et al., 2012]. The flask and in situ data for the South Pole and Mauna Loa sampling sites are from Keeling et al. [2005].

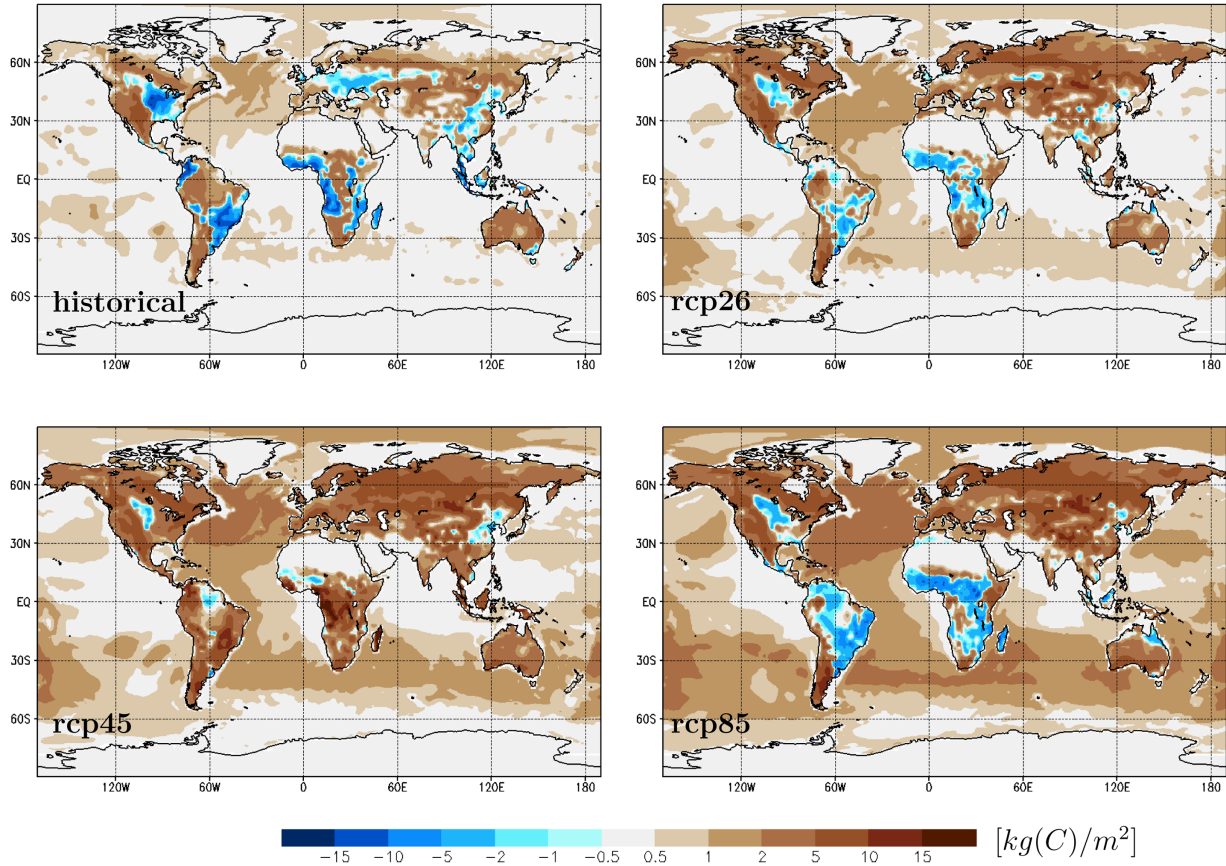


**Figure 16.** Change in carbon storage in  $\text{kgC}/\text{m}^2$  during the *historical* simulation (1850–2005) and *rcp26*, *rcp45*, and *rcp85* simulations (2006–2100) on land and in the ocean.

waters. Accordingly, the net  $\text{CO}_2$  sink areas are located in the North Atlantic and the North Pacific. Net source areas are located in the equatorial ocean and in carbon rich upwelling regions. The Southern Ocean, while being a net sink for atmospheric  $\text{CO}_2$ , exhibits large spatial variability affected by mesoscale eddies.

[72] The annual global flux of  $\text{CO}_2$  into the ocean calculated in both MPI-ESM-LR *esmHistorical* and *historical* simulations for the 1990s is about 2 PgC per year, which is in agreement with available estimates [Le Quéré *et al.*, 2009]. The experiment *esmHistorical*, however, exhibits a 25% larger interannual variability (expressed by the standard deviation) compared to that of the *historical* simulation [Ilyina *et al.*, 2013]. In the 21st century, as atmospheric  $\text{CO}_2$  concentrations grow, the oceanic uptake of  $\text{CO}_2$  increases in all future projections simulated with MPI-ESM. Yet, even in a high- $\text{CO}_2$  world, such as for instance projected under the RCP8.5 scenario, the model simulates  $\text{CO}_2$  uptake and outgassing regions in the ocean.

[73]  $\text{CO}_2$  taken up at the sea surface is transported into the ocean interior. Colder waters have a lower buffering capacity (a mechanism which, by a number of chemical reactions, converts atmospheric  $\text{CO}_2$  into forms not further available for air-sea exchange [cf. Zeebe and Wolf-Gladrow, 2001]) than warmer waters. This, together with the general thermohaline circulation

pattern, shapes the ocean water column carbon storage projected in MPI-ESM experiments (Figure 16). Despite its relatively small volume, the North Atlantic between  $40^\circ\text{N}$  and  $60^\circ\text{N}$ , displays the largest changes in the vertically integrated carbon inventory already during the “historical” time period being in agreement with observations-based assessments [e.g., Sabine *et al.*, 2004]. The storage of anthropogenic carbon increases in future projections in MPI-ESM depending on the amount of carbon available for the oceanic uptake, i.e., being smallest in *rcp26* and largest in *rcp85*. Also the southern hemisphere oceans (between about  $15^\circ\text{S}$  and  $60^\circ\text{S}$ ) accumulate substantial amounts of carbon as atmospheric  $\text{CO}_2$  increases. In contrast, the carbon inventory change of the North Pacific is considerably smaller. The model projects smallest changes in the carbon content of the Indian Ocean and in the equatorial Pacific Ocean. Likewise, changes projected by the model in the Southern Ocean’s (south of  $60^\circ\text{S}$ ) carbon content are relatively small. Besides, there are large uncertainties associated with the future evolution of the Southern Ocean carbon sink [e.g., Tjiputra *et al.*, 2010].

#### 6.4. Land Carbon Uptake

[74] Terrestrial ecosystems currently serve as a net sink of anthropogenic  $\text{CO}_2$  emissions. For the last three decades of the 20th century in the *historical* simulation the

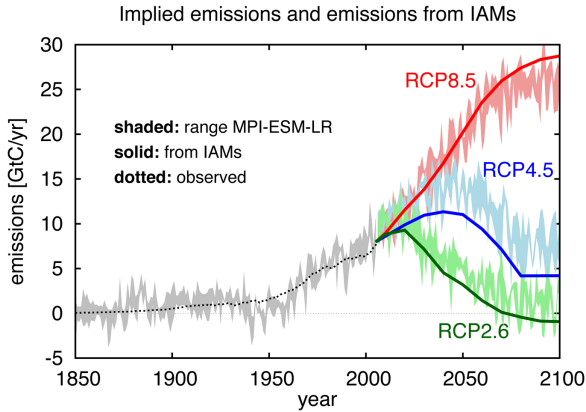


**Figure 17.** Compatible  $\text{CO}_2$  emissions. The shaded area displays the range of compatible emissions as obtained from the three ensemble members in *historical* and *rcp26*, *rcp45*, and *rcp85* simulations. The dotted line depicts the historical emissions from fossil fuel combustion [Andres et al., 2009], and the colored lines show emissions from fossil fuel combustion, as obtained from the integrated assessment models [IIASA RCP database at <http://www.iiasa.ac.at/web-apps/tnt/RcpDb>].

land uptake is on average 3.2 GtC/year, which is at the upper side of observation-based estimates of  $2.3 \pm 1.0$  GtC/year [Le Quéré et al., 2009]. The strength of the land carbon uptake is influenced by many factors: First, biomass and soil carbon storages are changed due to anthropogenic land use and land cover changes. The increase in atmospheric  $\text{CO}_2$  concentration (“ $\text{CO}_2$  fertilization”) leads to additional carbon assimilation in photosynthesis. At the same time, elevated temperatures cause changes in plant productivity, autotrophic and heterotrophic (soil) respiration. Also changes in precipitation modify plant productivity. Finally, changes in climate,  $\text{CO}_2$ , and natural disturbances such as fires lead to shifts in the distribution of natural vegetation cover.

[75] A combination of these processes explains the geographically resolved changes in land carbon seen in Figure 16. In the *historical* simulation, the regions of carbon loss are identical with the regions of strong agricultural expansion. Due to  $\text{CO}_2$  fertilization additional carbon is stored in rural regions and regions with a lower level of land use conversions. In *rcp26* and *rcp85*, the pattern of carbon gains and losses is rather similar, although in strength gains and losses are different. This similarity is partly explained by the ongoing deforestation in similar regions in both scenarios. In the tropics and subtropics, the increase in temperature follows the reduction in precipitation and there both act to reduce land carbon. Therefore, in the tropics and subtropics the patterns of carbon changes closely follow the patterns of precipitation decrease (compare Figure 10). In these regions, forests are replaced by shrublands or savanna-type vegetation. This vegetation shift is particularly strong in Brazil and middle and southern Africa. The smaller extent of regions of carbon loss in *rcp26* is explained by a

smaller reduction in vegetation than in *rcp85*. In both simulations due to the temperature increase especially in the boreal regions forests are shifted northward leading there to increased carbon storage. The differences in carbon storage between these two simulations and *rcp45* are largely a result of the strong reforestation in this latter scenario. Thereby large regions of carbon loss seen in *rcp26* and *rcp85* are converted into regions of carbon gain. In the remaining regions of carbon loss the effect of temperature increase and droughts overpowers the reforestation and  $\text{CO}_2$  fertilization effects. In total, the land remains a net carbon sink in all scenarios. Note that the land carbon model had not accounted for nitrogen or phosphorus limitations, which may considerably reduce the land carbon uptake in the future [e.g., Goll et al., 2012]. More details on the effect of land use change in these simulations can be found in Brovkin et al. [2013].

## 6.5. Compatible Emissions

[76] The carbon cycle is included in all MPI-ESM simulations so that the  $\text{CO}_2$  exchange flux between the atmosphere and the land and ocean, respectively, is simulated interactively, based on the processes represented in the model. However, in the *historical* and the *rcp26*, *rcp45*, and *rcp85* simulations the time-dependent atmospheric  $\text{CO}_2$  concentration is prescribed. The sum of carbon changes in land and ocean inventories and the prescribed increase of the atmospheric carbon inventory equals to the “compatible  $\text{CO}_2$  emission,” which can be interpreted as the fossil fuel emission that fits to the prescribed transient atmospheric  $\text{CO}_2$  concentration and the modeled  $\text{CO}_2$  exchange flux between the atmosphere and the land and ocean. Figure 17 depicts the diagnosed compatible  $\text{CO}_2$  emissions for the *historical*, *rcp26*, *rcp45*, and *rcp85* simulations, following the description in Roeckner et al. [2011].

[77] For the historical period the compatible emissions agree well with the known fossil fuel emissions. Reasonable agreement is also found with the emission calculations from the IAMs (integrated assessment models) for the different RCPs, although especially for the strong reforestation scenario RCP4.5 our simulations allow for about 30% higher peak emissions. The origin of this discrepancy could probably only be identified by an in depth comparison of the process descriptions in MPI-ESM and the IAM MiniCAM by which RCP4.5 was constructed. Also for *rcp26* our simulations give a more optimistic result for the total amount of compatible emissions, which is roughly 1.5 times the historic (1850–2005) fossil fuel emissions. However, for *rcp85* scenario, the compatible emissions are less than the IAM emissions (red line in Figure 17). This is in line with simulations of the other CMIP5 ESMs with interactive carbon cycle [Jones et al., 2013].

## 7. Summary and Conclusions

[78] The new Max-Planck-Institute Earth System Model MPI-ESM has been employed for a large suite of CMIP5 simulations. This study presents the core experiments for the estimation of climate sensitivity and

transient climate change, and the transient experiments from 1850 to 2005 based on observed forcings and for 2006 to 2100, and in part to 2300, for the representative concentration pathway scenarios with radiative forcings of 2.6, 4.5, and 8.5 W/m<sup>2</sup> in 2100 (RCP2.6, RCP4.5, and RCP8.5). The study makes use of the simulations based on the MPI-ESM-LR model configuration. The evaluation focuses on the model performance in the historic period, the physical climate change properties as diagnosed from the coupled experiments with idealized or complex forcing, and the carbon cycle.

[79] The overall performance of the MPI-ESM-LR, based on a modified Reichler-Kim standardized error, is better than that of the older ECHAM5/MPIOM model, mainly due to improvements of the extratropical circulation. Still maps of systematic errors in key parameters like annual mean surface temperature and precipitation show similar structures and amplitudes as is in older model versions, as for instance a cold bias in equatorial Pacific SST or warm biases in the subtropical ocean basins, where stratocumulus is insufficiently simulated. Precipitation biases occur accordingly. Precipitation differences in South America and in Africa are clearly related to the net primary productivity and consequently to the surface albedo. MPI-ESM-LR is capable of simulating the main modes of tropical variability as shown for the Madden-Julian Oscillation and El Niño.

[80] Climate sensitivity is assessed in the *abrupt4xCO<sub>2</sub>* experiment through the regression of the radiative forcing at TOA and the near surface air temperature. Here, it is found that no single climate sensitivity exists for this model system. Instead a transition occurs in the climate feedback at a global warming of about 5°C, separating two regimes with linear equilibrations, thus with separate climate feedback parameters. As the feedback parameter of the second regime is smaller, the extrapolation from this regime results in a significantly higher equilibrium temperature for CO<sub>2</sub> quadrupling than the extrapolation from the first regime. Climate feedback parameters estimated from *piControl*, *rcp45*, and *rcp85* fall between the values found for *abrupt4xCO<sub>2</sub>*. A separate analysis of the shortwave and longwave components of the feedback parameter shows that the longwave component generally weakens in a warming climate. The shortwave component can increase or decrease, depending on the nature of the experiment and the amount of warming.

[81] The idealized climate change experiment, driven by a 1% increase in CO<sub>2</sub> concentration per year, yields a transient climate change of 2.0°C over the first CO<sub>2</sub> doubling and of further 3.1°C over the second CO<sub>2</sub> doubling. The reason for the increase in TCR for MPI-ESM-LR must be sought in a considerable weakening of the ocean heat uptake efficiency in the warmer years.

[82] The precipitation sensitivity is found to be highest (+2.5% K<sup>-1</sup>) in the *abrupt4xCO<sub>2</sub>* simulation, where the direct CO<sub>2</sub> effect on the atmospheric heating that tends to reduce precipitation remains essentially constant, and lowest in the *rcp85* and *1pctCO<sub>2</sub>* experiments (1.6% K<sup>-1</sup>), which have a strongly increasing CO<sub>2</sub> con-

centration, and thus an increasingly damping effect of CO<sub>2</sub> on the precipitation.

[83] From climatological 1850 conditions to 2005, the historical simulation warms from 13.5°C to 14.3°C. The warming is thus probably about 0.1°C stronger than in observations. Until 2080–2100, the warming compared to climatological 1850 conditions spans a range of 1.5° in *rcp26* to 4.4°C in *rcp85*. The goal of the RCP2.6 scenario, to limit the global warming to 2°C, thus is reached in this model system. Within the range resulting from the three scenarios the warming patterns scaled by the global warming are essentially independent of the global warming. While the latitudes from the equator to 50°N warm as the global average, the higher northern latitudes warm about 2.2 times stronger and the high southern latitude oceans warm about one third of the global mean. Also patterns of precipitation change in the different scenarios show a high similarity if scaled by the global mean warming. Thus, the typical response patterns in temperature and precipitation seem quite robust over the range of RCP scenarios used here.

[84] All MPI-ESM simulations have been performed with a prognostic global carbon cycle, although only in the esm simulations the ocean and land portions of the global carbon cycle were coupled via prognostic CO<sub>2</sub> in the atmosphere. This difference in coupling has consequences for the interannual variability of carbon storage on land and in the ocean. In the esm case, this variability causes land-driven changes in atmospheric CO<sub>2</sub>, which are partially damped by the ocean carbon uptake or release, but also induce negative feedbacks on land carbon uptake via changes in CO<sub>2</sub> fertilization. As a consequence, in the esm simulations interannual variability in land carbon storage is smaller than in uncoupled simulations, whereas variability in ocean carbon storage is larger in the esm simulations than in the uncoupled simulations (compare Ilyina et al. [2013]).

[85] For the *esmHistorical* and *historical* simulations, global land and ocean CO<sub>2</sub> fluxes are in agreement with observations. This is visible not only from the good fit between observed historical atmospheric CO<sub>2</sub> and simulated atmospheric CO<sub>2</sub> in the *esmHistorical* simulation, but also from the calculation of compatible emissions for the historical simulation. Concerning the *rcp* simulations, the overall development of compatible emissions calculated from MPI-ESM-LR agrees with the fossil fuel emissions projected by the IAMs. Nevertheless, quantitative differences exist. In particular, for RCP2.6, which is the scenario motivated by the internationally accepted 2 K target, cumulative compatible emissions from 2005 to 2100 from MPI-ESM are by a factor of approximately 1.5 higher than expected from the IMAGE model, from which the RCP2.6 scenario was derived. However, for the RCP8.5 scenario, the compatible emissions, in particular after year 2050, are significantly less than the IAM emissions.

[86] **Acknowledgments.** Computational resources were made available by Deutsches Klimarechenzentrum (DKRZ) through support from the Bundesministerium für Bildung und Forschung (BMBF). The research leading to these results has also received funding from

the European Union, Seventh Framework Programme (FP7/2007–2013) in the COMBINE project under grant agreement 226520.

## References

- Ahn, J., E. J. Brook, L. Mitchell, J. Rosen, J. R. McConnell, K. Taylor, D. Etheridge, and M. Rubino (2012), Atmospheric CO<sub>2</sub> over the last 1000 years: A high-resolution record from the West Antarctic Ice Sheet (WAIS) Divide ice core, *Global Biogeochem. Cycles*, 26, GB2027, doi:10.1029/2011GB004247.
- Allen, M. R., and W. J. Ingram (2002), Constraints on future changes in climate and the hydrologic cycle, *Nature*, 419, 224–232.
- Andres, R. J., T. A. Boden, and G. Marland (2009), Annual fossil-fuel CO<sub>2</sub> emissions: Mass of emissions gridded by one degree latitude by one degree longitude, Carbon Dioxide Inf. Anal. Cent., Oak Ridge Natl. Lab., U.S. Dep. of Energy, Oak Ridge, Tenn., doi:10.3334/CDIAC/ffe.ndp058.2009.
- Andrews, T., J. M. Gregory, M. J. Webb, and K. E. Taylor (2012), Forcing, feedbacks and climate sensitivity in CMIP5 coupled atmosphere-ocean climate models, *Geophys. Res. Lett.*, 39, L09712, doi:10.1029/2012GL051607.
- Arrhenius, S. (1896), On the influence of carbonic acid in the air upon the temperature of the ground, *J. Sci.*, 41, 237–275.
- Block, K., and T. Mauritsen, (2013), Forcing and feedback in the MPI-ESM-LR coupled model under abruptly quadrupled CO<sub>2</sub>, *J. Adv. Model. Earth Syst.*, doi: 10.1002/jame.20041, accepted.
- Bony, S., G. Bellon, D. Klocke, S. Sherwood, S. Fergepin, and S. Denavit (2013), Robust direct effect of carbon dioxide on tropical circulation and regional precipitation, *Nat. Geosci.*, 6, 447–451.
- Bretagnon, P., and G. Francou (1988), Planetary theories in rectangular and spherical variables—VSOP 87 solutions, *Astron. Astrophys.*, 202, 309–315.
- Brovkin, V., T. Raddatz, C. H. Reick, M. Claussen, and V. Gayler (2009), Global biogeophysical interactions between forest and climate, *Geophys. Res. Lett.*, 36, L07405, doi:10.1029/2009GL037543.
- Brovkin, V., et al. (2013), Effect of anthropogenic land-use and land cover changes on climate and land carbon storage in CMIP5 projections for the 21st century, *J. Clim.*, doi:10.1175/JCLI-D-12-00623.1.
- Cess, R. D., et al. (1989), Interpretation of cloud-climate feedback as produced by atmospheric general circulation models, *Science*, 245, 513–516.
- Cionni, I., V. Eyring, J. F. Lamarque, W. J. Randel, D. S. Stevenson, F. Wu, G. E. Bodeker, T. G. Shepherd, D. T. Shindell, and D. W. Waugh (2011), Ozone database in support of CMIP5 simulations: Results and corresponding radiative forcing, *Atmos. Chem. Phys.*, 11, 11,267–11,292, doi:10.5194/acp-11-11267-2011.
- Crueger, T., B. Stevens, and R. Brokopf (2012), The Madden-Julian Oscillation in ECHAM6 and the introduction of an objective MJO metric, *J. Clim.*, 26, 3241–3257, doi:10.1175/JCLI-D-12-00413.1.
- Etheridge, D. M., L. P. Steele, R. L. Langenfelds, R. J. Francey, J.-M. Barnola, and V. I. Morgan (1996), Natural and anthropogenic changes in atmospheric CO<sub>2</sub> over the last 100 years from air in Antarctic ice and firn, *J. Geophys. Res.*, 101, 4115–4128, doi:10.1029/95JD03410.
- Eyring, V., et al. (2010), Multi-model assessment of stratospheric ozone return dates and ozone recovery in CCMVal-2 models, *Atmos. Chem. Phys.*, 10, 9451–9472, doi:10.5194/acp-10-9451-2010.
- Forest, C. E., P. H. Stone, and A. P. Sokolov (2008), Constraining climate model parameters from observed 20th century changes, *Tellus, Ser. A*, 60, 911–920, doi:10.1111/j.1600-0870.2008.00346.x.
- Friedlingstein, P., et al. (2006), Climate-carbon cycle feedback analysis: Results from the C4MIP model intercomparison, *J. Clim.*, 19, 3337–3353, doi:10.1175/JCLI3800.1.
- Gates, W. L., et al. (1999), An overview of the results of the Atmospheric Model Intercomparison Project (AMIP I), *Bull. Am. Meteorol. Soc.*, 80, 29–55.
- Giorgetta, M. A., E. Manzini, E. Roeckner, M. Esch, and L. Bengtsson (2006), Climatology and forcing of the quasi-biennial oscillation in the MAECHAM5 model, *J. Clim.*, 19, 3882–3901, doi:10.1175/JCLI3830.1.
- Giorgetta, M., et al. (2012a), *CMIP5 Simulations of the Max Planck Institute for Meteorology (MPI-M) Based on the MPI-ESM-LR Model: The piControl Experiment, Served by ESGF*, World Data Cent. for Clim, doi: 10.1594/WDCC/CMIP5.MXELpc, WDCC, DKRZ.
- Giorgetta, M., et al. (2012b), *CMIP5 Simulations of the Max Planck Institute for Meteorology (MPI-M) Based on the MPI-ESM-LR Model: The abrupt4xCO<sub>2</sub> Experiment, Served by ESGF*, World Data Cent. for Clim, doi: 10.1594/WDCC/CMIP5.MXELc2, WDCC, DKRZ.
- Giorgetta, M., et al. (2012c), *CMIP5 Simulations of the Max Planck Institute for Meteorology (MPI-M) Based on the MPI-ESM-LR Model: The 1pctCO<sub>2</sub> Experiment, Served by ESGF*, World Data Cent. for Clim, doi: 10.1594/WDCC/CMIP5.MXELc1, WDCC, DKRZ.
- Giorgetta, M., et al. (2012d), *CMIP5 Simulations of the Max Planck Institute for Meteorology (MPI-M) Based on the MPI-ESM-LR Model: The Historical Experiment, Served by ESGF*, World Data Cent. for Clim, doi: 10.1594/WDCC/CMIP5.MXELhi, WDCC, DKRZ.
- Giorgetta, M., et al. (2012e), *CMIP5 Simulations of the Max Planck Institute for Meteorology (MPI-M) Based on the MPI-ESM-LR Model: The anip Experiment, Served by ESGF*, World Data Cent. for Clim, doi: 10.1594/WDCC/CMIP5.MXELam, WDCC, DKRZ.
- Giorgetta, M., et al. (2012f), *CMIP5 Simulations of the Max Planck Institute for Meteorology (MPI-M) Based on the MPI-ESM-LR Model: The rcp26 Experiment, Served by ESGF*, World Data Cent. for Clim, doi: 10.1594/WDCC/CMIP5.MXELr2, WDCC, DKRZ.
- Giorgetta, M., et al. (2012g), *CMIP5 Simulations of the Max Planck Institute for Meteorology (MPI-M) Based on the MPI-ESM-LR Model: The rcp45 Experiment, Served by ESGF*, World Data Cent. for Clim, doi: 10.1594/WDCC/CMIP5.MXELr4, WDCC, DKRZ.
- Giorgetta, M., et al. (2012h), *CMIP5 Simulations of the Max Planck Institute for Meteorology (MPI-M) Based on the MPI-ESM-LR Model: The rcp85 Experiment, Served by ESGF*, World Data Cent. for Clim, doi: 10.1594/WDCC/CMIP5.MXELr8, WDCC, DKRZ.
- Gleckler, P. J., K. AchutaRao, J. M. Gregory, B. D. Santer, K. E. Taylor, and T. M. L. Wigley, (2006), Krakatoa lives: The effect of volcanic eruptions on ocean heat content and thermal expansion, *Geophys. Res. Lett.*, 33, L17702, doi:10.1029/2006GL026771.
- Goll, D., V. Brovkin, B. Parida, C. H. Reick, J. Kattge, P. B. Reich, P. M. van Bodegom, and Ü. Niinemets (2012), Nutrient limitation reduces land carbon uptake in simulations with a model of combined carbon, nitrogen and phosphorus cycling, *Biogeosciences*, 9, 3547–3569, doi:10.5194/bg-9-3547-2012.
- Gregory, J. M., W. J. Ingram, M. A. Palmer, G. S. Jones, P. A. Stott, R. B. Thorpe, J. A. Lowe, T. C. Johns, and K. D. Williams (2004), A new method for diagnosing radiative forcing and climate sensitivity, *Geophys. Res. Lett.*, 31, L03205, doi:10.1029/2003GL018747.
- Gregory, J. M., et al. (2013), Climate models without pre-industrial volcanic forcing underestimate historical ocean thermal expansion, *Geophys. Res. Lett.*, 40, 1600–1604, doi:10.1002/grl.50339.
- Hagemann, S., and L. Dümenil-Gates (2003), An improved sub grid runoff parameterization scheme for climate models, *Clim. Dyn.*, 21, 349–359.
- Hagemann, S., A. Loew, and A. Andersson (2013), Combined evaluation of MPI-ESM land surface water and energy fluxes, *J. Adv. Model. Earth Syst.*, doi:10.1029/2012MS000173.
- Hansen, J., M. Sato, P. Kharecha, and K. von Schuckmann (2011), Earth's energy imbalance and implications, *Atmos. Chem. Phys.*, 11, 13,421–13,449, doi:10.5194/acp-11-13421-2011.
- Held, I. M., and B. J. Soden (2006), Robust responses of the hydrological cycle to global warming, *J. Clim.*, 19, 5686–5699, doi:10.1175/JCLI3990.1.
- Holland, M. M., and C. M. Bitz (2003), Polar amplification of climate change in coupled models, *Clim. Dyn.*, 21, 221–232, doi:10.1175/1520-0493(1999)127%3C2204:FASOCR%3E2.0.CO;2.
- Huang, J., and M. B. McElroy, (2012), The contemporary and historical budget of atmospheric CO<sub>2</sub>, *Can. J. Physics*, 90, 707–716, doi: 10.1139/p2012-033.
- Hurtt, G. C., S. Frolking, M. G. Fearon, B. Moore, E. Sheviakova, S. Malyshev, S. W. Pacala, and R. A. Houghton (2006), The underpinnings of land-use history: Three centuries of global gridded land-use transitions, wood-harvest activity, and resulting secondary lands, *Global Change Biol.*, 12, 1208–1229.
- Hurtt, G. C., et al. (2011), Harmonization of land-use scenarios for the period 1500–2100: 600 years of global gridded annual land-use

- transitions, wood harvest, and resulting secondary lands, *Clim. Change*, 109, 117–161, doi:10.1007/s10584-011-0153-2.
- Iacono, M. J., J. S. Delamere, E. J. Mlawer, M. W. Shephard, S. A. Clough, and W. D. Collins (2008), Radiative forcing by long-lived greenhouse gases: Calculations with the AER radiative transfer models, *J. Geophys. Res.*, 113, D13103, doi:10.1029/2008JD009944.
- Ilyina, T., K. Six, J. Segschneider, E. Maier-Reimer, H. Li, and I. Núñez-Riboni (2013), Global ocean biogeochemistry model HAMOCC: Model architecture and performance as component of the MPI-Earth System Model in different CMIP5 experimental realizations, *J. Adv. Model. Earth Syst.*, doi:10.1029/2012MS000178.
- Johns, T. C., et al. (2011), Climate change under aggressive mitigation: The ENSEMBLES multi-model experiment, *Clim. Dyn.*, 37, 1975–2003, doi:10.1007/s00382-011-1005-5.
- Jones, P. W. (1999), First- and second-order conservative remapping schemes for grids in spherical coordinates, *Mon. Weather Rev.*, 127, 2204–2210, doi:10.1175/1520-0493(1999)127<2204:FASOCR>2.0.CO;2.
- Jones, C., et al. (2013), Twenty-First century compatible CO<sub>2</sub> emissions and airborne fraction simulated by CMIP5 Earth System models under four representative concentration pathways, *J. Clim.*, doi:10.1175/JCLI-D-12-00554.1.
- Jungclaus, J. H., N. Keenlyside, M. Botzet, H. Haak, J.-J. Luo, M. Latif, J. Marotzke, U. Mikolajewicz, and E. Roeckner (2006), Ocean circulation and tropical variability in the coupled model ECHAM5/MPI-OM, *J. Clim.*, 19, 3952–3972.
- Jungclaus, J. H., et al. (2010), Climate and carbon-cycle variability over the last millennium, *Clim. Past*, 6, 723–737.
- Jungclaus, J. H., N. Fischer, H. Haak, K. Lohmann, J. Marotzke, D. Matei, U. Mikolajewicz, D. Notz, and J. S. von Storch (2013), Characteristics of the ocean simulations in MPIOM, the ocean component of the MPI-Earth System Model, *J. Adv. Model. Earth Syst.*, doi:10.1002/jame.20023.
- Kalnay, E., et al. (1996), The NCEP/NCAR 40-year reanalysis project, *Bull. Am. Meteorol. Soc.*, 77, 437–471.
- Karpechko, A. Y., and E. Manzini (2012), Stratospheric influence on tropospheric climate change in the Northern Hemisphere, *J. Geophys. Res.*, 117, D05133, doi:10.1029/2011JD017036.
- Keeling, D. D., T. P. Whorf, and the Carbon Dioxide Research Group (2005), *Atmospheric CO<sub>2</sub> concentrations (ppmv) derived from flask and in situ air samples collected at the South Pole and at Mauna Loa*, Scripps Inst. of Oceanogr., Univ. of Calif., San Diego, La Jolla.
- Key, R. M., A. Kozyr, C. L. Sabine, K. Lee, R. Wanninkhof, J. L. Bullister, R. A. Feely, F. J. Millero, C. Mordy, and T.-H. Peng (2004), A global ocean carbon climatology: Results from Global Data Analysis Project (GLODAP), *Global Biogeochem. Cycles*, 18, GB4031, doi:10.1029/2004GB002247.
- Kinne, S., O'Donnell, D., P. Stier, S. Kloster, K. Zhang, H. Schmidt, S. Rast, M. Giorgetta, T. F. Eck, and B. Stevens, (2013), HAC-v1: A new global aerosol climatology for climate studies, *J. Adv. Model. Earth Syst.*, 2013, doi: 10.1002/jame.20035, accepted.
- Krismer, T. R., M. A. Giorgetta, and M. Esch (2013), Seasonal aspects of the quasi-biennial oscillation in MPI-ESM and ERA-40, *J. Adv. Model. Earth Syst.*, 5, 1–16, doi:10.1002/jame.20024.
- Kuhlbrodt, T., and J. M. Gregory (2012), Ocean heat uptake and its consequence for the magnitude of sea level rise and climate change, *Geophys. Res. Lett.*, 39, L18608, doi:10.1029/2012GL052952.
- Lambert, S. J., and G. J. Boer (2001), CMIP1 evaluation and intercomparison of coupled climate models, *Clim. Dyn.*, 17, 83–106.
- Lambert, F. H., and M. J. Webb (2008), Dependency of global mean precipitation on surface temperature, *Geophys. Res. Lett.*, 35, L16706, doi:10.1029/2008GL034838.
- Le Quéré et al. (2009), Trends in the sources and sinks of carbon dioxide, *Nat. Geosci.*, 2, 831–836, doi:10.1038/ngeo689.
- Levitus, S., et al. (2012), World ocean heat content and thermosteric sea level change (0–2000 m), 1955–2010, *Geophys. Res. Lett.*, 39, L10603, doi:10.1029/2012GL051106.
- Li, C., J.-S. V. Storch, and J. Marotzke (2012), Deep-ocean heat uptake and equilibrium climate response, *Clim. Dyn.*, 40, 1071–1086, doi:10.1007/s00382-012-1350-z.
- Liebmann, B., and C. Smith (1996), Description of a complete (interpolated) OLR dataset, *Bull. Am. Meteorol. Soc.*, 77, 1275–1277.
- Lin, J.-L., et al. (2006), Tropical intraseasonal variability in 14 IPCC AR4 climate models. Part I: Convective Signals, *J. Clim.*, 19, 2665–2690.
- Lyman, J. M., S. A. Good, V. V. Gouretski, M. Ishii, G. C. Johnson, M. D. Palmer, D. M. Smith, and J. K. Willis (2010), Robust warming of the global upper ocean, *Nature*, 465, 334–337, doi:10.1038/nature09043.
- MacFarling, M. C., D. Etheridge, C. Trudinger, P. Steele, R. Langenfelds, T. van Ommen, A. Smith, and J. Elkins (2006), Law dome CO<sub>2</sub>, CH<sub>4</sub> and N<sub>2</sub>O ice core records extended to 2000 years BP, *Geophys. Res. Lett.*, 33, L14810, doi:10.1029/2006GL026152.
- Madden, R. A., and P. R. Julian (1971), Detection of a 40–50 day oscillation in the zonal wind in the tropical Pacific, *J. Atmos. Sci.*, 28, 702–708, doi:10.1175/1520-0469(1971)028<0702:DOADOI>2.0.CO;2.
- Maier-Reimer, E., and K. Hasselmann (1987), Transport and storage of CO<sub>2</sub> in the ocean—An inorganic ocean circulation carbon cycle model, *Clim. Dyn.*, 2, 63–90.
- Manzini, E., M. Giorgetta, M. Esch, L. Kornblueh, and E. Roeckner (2006), The influence of sea surface temperatures on the northern winter stratosphere: Ensemble simulations with the MAECHAM5 model, *J. Clim.*, 19(16), 3863–3881.
- Matsumoto, K., and N. Gruber (2005), How accurate is the estimation of anthropogenic carbon in the ocean? An evaluation of the ΔC\* method, *Global Biogeochem. Cycles*, 19, GB3014, doi:10.1029/2004GB002397.
- Mauritsen, T., et al. (2012), Tuning the climate of a global model, *J. Adv. Model. Earth Syst.*, 4, M00A01, doi:10.1029/2012MS000154.
- Meinshausen, M., et al. (2011), The RCP greenhouse gas concentrations and their extension from 1765 to 2300, *Clim. Change*, 109, 213–241, doi:10.1007/s10584-011-0156-z, 2011.
- Mitchell, J. F., C. A. Wilson, and W. M. Cunningham (1987), On CO<sub>2</sub> climate sensitivity and model dependence of results, *Q. J. R. Meteorol. Soc.*, 113, 293–322, doi:10.1002/qj.49711347517.
- Möbis, B., and B. Stevens (2012), Factors controlling the position of the ITCZ on an Aquaplanet, *J. Adv. Model. Earth Syst.*, 4, M00A04, doi:10.1029/2012MS000199.
- Moss, R., et al. (2010), The next generation of scenarios for climate change research and assessment, *Nature*, 463, 747–756, doi:10.1038/nature08823.
- Nakicenovic, N., et al. (2000), *Special Report on Emissions Scenarios: A Special Report of Working Group III of the Intergovernmental Panel on Climate Change*, Cambridge Univ. Press, Cambridge, U. K.
- Notz, D., F. A. Haumann, H. Haak, J. H. Jungclaus, and J. Marotzke (2013), Arctic sea-ice evolution as modeled by MPI-ESM, *J. Adv. Model. Earth Syst.*, 5, 1–22, doi:10.1002/jame.20016.
- O'Gorman, P. A., and T. Schneider (2008), The hydrological cycle over a wide range of climates simulated with an Idealized GCM, *J. Clim.*, 21, 3815–3832, doi:10.1175/2007JCLI2065.1.
- Pongratz, J., C. Reick, T. Raddatz, and M. Claussen (2008), A reconstruction of global agricultural areas and land cover for the last millennium, *Global Biogeochem. Cycles*, 22, GB3018, doi:10.1029/2007GB003153.
- Pongratz, J., C. H. Reick, T. Raddatz, and M. Claussen (2009), Effects of anthropogenic land cover change on the carbon cycle of the last millennium, *Global Biogeochem. Cycles*, 23, GB4001, doi:10.1029/2009GB003488.
- Randall, D. A., et al. (2007), Climate models and their evaluation, in *Climate Change 2007: The Physical Science Basis, Contribution of Working Group I to the Fourth Assessment Report of the Intergovernmental Panel on Climate Change*, edited by S. Solomon, et al, Cambridge Univ. Press, Cambridge, U. K., 589–662.
- Rayner, N. A., D. E. Parker, E. B. Horton, C. K. Folland, L. V. Alexander, D. P. Rowell, E. C. Kent, and A. Kaplan (2003), Global analyses of sea surface temperature, sea ice, and night marine air temperature since the late nineteenth century, *J. Geophys. Res.*, 108(D14), 4407, doi:10.1029/2002JD002670.
- Reick, C., et al. (2012a), *CMIP5 Simulations of the Max Planck Institute for Meteorology (MPI-M) Based on the MPI-ESM-LR Model: The esmControl Experiment, Served by ESGF*, World Data Cent. for Clim, doi: 10.1594/WDCC/CMIP5.MXElec, WDCC, DKRZ.
- Reick, C., et al. (2012b), *CMIP5 Simulations of the Max Planck Institute for Meteorology (MPI-M) Based on the MPI-ESM-LR Model: The esmHistorical Experiment, Served by ESGF*, World Data Cent. for Clim, doi: 10.1594/WDCC/CMIP5.MXELeh, WDCC, DKRZ.
- Reick, C., et al. (2012c), *CMIP5 Simulations of the Max Planck Institute for Meteorology (MPI-M) Based on the MPI-ESM-LR Model: The esmFuture Experiment, Served by ESGF*, World Data Cent. for Clim, doi: 10.1594/WDCC/CMIP5.MXEFor, WDCC, DKRZ.

- esmrcp85 Experiment, Served by ESGF*, World Data Cent. for Clim, doi: 10.1594/WDCC/CMIP5.MXELe8.], WDCC, DKRZ.
- Reick, C. H., T. Raddatz, V. Brovkin, and V. Gayler (2013), The representation of natural and anthropogenic land cover change in MPI-ESM, *J. Adv. Model. Earth Syst.*, 5, 1–24, doi:10.1002/jame.20022.
- Riahi, K., V. Krey, S. Rao, V. Chirkov, G. Fischer, P. Kolp, G. Kindermann, N. Nakicenovic, and P. Rafai (2011), RCP-8.5: Exploring the consequence of high emission trajectories, *Clim. Change*, 109, 33–57, doi:10.1007/s10584-011-0149-y.
- Richter, I., and S.-P. Xie (2008), On the origin of equatorial Atlantic biases in coupled general circulation models, *Clim. Dyn.*, 31, 587–598, doi:10.1007/s00382-008-0364-z.
- Roeckner, E., et al. (2003), *The atmospheric general circulation model ECHAM5. Part I: Model description*, Tech. Rep. 349, 127 pp., MPI for Meteorol., Hamburg, Germany.
- Roeckner, E., R. Brokopf, M. Esch, M. Giorgi, S. Hagemann, L. Kornblueh, E. Manzini, U. Schlese, and U. Schulzweida (2006), Sensitivity of simulated climate to horizontal and vertical resolution in the ECHAM5 atmosphere model, *J. Clim.*, 19, 3771–3791.
- Roeckner, E., M. A. Giorgi, T. Crueger, M. Esch, and J. Pongratz (2011), Historical and future anthropogenic emission pathways derived from coupled climate-carbon cycle simulations, *Clim. Change*, 105, 91–108, doi:10.1007/s10584-010-9886-6.
- Roeckner, E., T. Mauritsen, M. Esch, and R. Brokopf (2012), Impact of melt ponds on Arctic sea ice in past and future climates as simulated by MPI-ESM, *J. Adv. Model. Earth Syst.*, 4, M00A02, doi:10.1029/2012MS000157.
- Sabine, C. L., et al. (2004), The oceanic sink for anthropogenic CO<sub>2</sub>, *Science*, 305, 367–371, doi:10.1126/science.1097403.
- Sato, N., C. Takahashi, A. Seiki, K. Yoneyama, R. Shirooka, and Y. N. Takayabu (2009), An evaluation of the reproducibility of the Madden-Julian Oscillation in the CMIP3 multi-models, *J. Meteorol. Soc. Jpn.*, 87, 791–805.
- Schmidt, H., et al. (2012), The response of the middle atmosphere to anthropogenic and natural forcing in the CMIP5 simulations with the MPI-ESM, *J. Adv. Model. Earth Syst.*, 5, 98–116, doi:10.1002/jame.20014.
- Schneck, R., C. H. Reick, and T. Raddatz (2013), The land contribution to natural CO<sub>2</sub> variability on time scales of centuries, *J. Adv. Model. Earth Syst.*, 5, 354–365, doi:10.1002/jame.20029.
- Schubert, J. J., B. Stevens, and T. Crueger (2013), Madden-Julian oscillation as simulated by the Max Planck Institute for Meteorology Earth System Model: Over the last and into the next millennium, *J. Adv. Model. Earth Syst.*, 5(1), 71–84.
- Schubert, J. J., B. Stevens, and T. Crueger (2013), Madden-Julian oscillation as simulated by the Max Planck Institute for Meteorology Earth System Model: Over the last and into the next millennium, *J. Adv. Model. Earth Syst.*, 5, 71–84, doi:10.1029/2012MS000180.
- Senior, C. A., and J. F. B. Mitchell (2000), The time-dependence of climate sensitivity, *Geophys. Res. Lett.*, 27, 2685–2688, doi:10.1029/2000GL011373.
- Sperber, K. R., S. Gualdi, S. Legutke, and V. Gayler (2005), The Madden-Julian oscillation in ECHAM4 coupled and uncoupled general circulation models, *Clim. Dyn.*, 25, 117–140.
- Stenchikov, G. L., I. Kirchner, A. Robock, H.-F. Graf, J. C. Antuña, R. G. Grainger, A. Lambert, and L. Thomason (1998), Radiative forcing from the 1991 Mount Pinatubo volcanic eruption, *J. Geophys. Res.*, 103, 13,837–13,857.
- Stevens, B., and S. Bony (2013), Water in the atmosphere, *Phys. Today*, 66(6), 29–34.
- Stevens, B., et al. (2013), Atmospheric component of the MPI-M Earth system model: ECHAM6, *J. Adv. Model. Earth Syst.*, 5, 146–172, doi:10.1002/jame.20015.
- Stier, P., et al. (2005), The aerosol-climate model ECHAM5-HAM, *Atmos. Chem. Phys.*, 5, 1125–1156.
- Stuber, N., M. Ponater, and R. Sausen, (2001), Is the climate sensitivity to ozone perturbations enhanced by stratospheric water vapor feedback? *Geophys. Res. Lett.*, 28, 2887–2890, doi: 10.1029/2001GL013000.
- Taylor, K. E., R. J. Stouffer, and G. A. Meehl (2009), A summary of the CMIP5 experiment design, PCMDI Report, 33 pp, PCMDI, Lawrence Livermore National Laboratory, Livermore, CA 94551-0808, United States. [Available at [http://cmip-pcmdi.llnl.gov/cmip5/docs/Taylor\\_CMIP5\\_design.pdf](http://cmip-pcmdi.llnl.gov/cmip5/docs/Taylor_CMIP5_design.pdf).]
- Taylor, K. E., R. J. Stouffer, and G. A. Meehl (2012), An overview of CMIP5 and the experiment design, *Bull. Am. Meteorol. Soc.*, 93, 485–498, doi:10.1175/BAMS-D-11-00094.1.
- Thomson, A. M., et al. (2011), RCP4.5: A pathway for stabilization of radiative forcing by 2100, *Clim. Change*, 109, 77–94, doi:10.1007/s10584-011-0151-4.
- Tjiputra, J. F., K. Assmann, and C. Heinze (2010), Anthropogenic carbon dynamics in the changing ocean, *Ocean Sci.*, 6, 605–614, doi:10.5194/os-6-605-010.
- Valcke, S. (2013), The OASIS3 coupler: A European climate modelling community software, *Geosci. Model Dev.*, 6, 373–388, doi:10.5194/gmd-6-373-2013, 2013.
- Van Vuuren, D. P., et al. (2011a), Representative concentration pathways: An overview, *Clim. Change*, 109, 5–31.
- Van Vuuren, D. P., et al. (2011b), RCP2.6: Exploring the possibility to keep global mean temperature change below 2°C, *Clim. Change*, 109, 95–116.
- Wahl, S., M. Latif, W. Park, and N. Keenlyside (2011), On the tropical Atlantic SST warm bias in the Kiel climate model, *Clim. Dyn.* 36, 891–906, doi:10.1007/s00382-009-0690-9.
- Waliser, D., et al. (2009), MJO simulation diagnostics, *J. Clim.*, 22, 3006–3030.
- Watanabe, M., Y. Kamae, M. Yoshimori, A. Oka, M. Sato, M. Ishii, T. Mochizuki, and M. Kimoto (2013), Strengthening of ocean heat uptake efficiency associated with the recent climate hiatus, *Geophys. Res. Lett.*, 40, 3175–3179, doi:10.1002/grl.50541.
- Winton, M. (2006), Does the Arctic sea ice have a tipping point?, *Geophys. Res. Lett.*, 33, L23504, doi:10.1029/2006GL028017.
- Winton, M., K. Takahashi, and I. M. Held (2010), Importance of ocean heat uptake efficacy to transient climate change, *J. Clim.*, 23, 2333–2344.
- Zeebe, R. E., and D. A. Wolf-Gladrow (2001), *CO<sub>2</sub> in Seawater: Equilibrium, Kinetics, Isotopes*, 346 pp., Elsevier, Amsterdam.
- Zhang, C. (2005), Madden-Julian oscillation, *Rev. Geophys.*, 43, RG2003, doi:10.1029/2004RG000158.

---

Corresponding author: M. A. Giorgi, Max-Planck-Institute für Meteorologie, Bundesstr. 53, DE-20146 Hamburg, Germany. (marco.giorgi@mpimet.mpg.de)